Nano Research

ISSN 1998-0124 CN 11-5974/O4
https://doi.org/10.26599/NR.2026.94908709

Review Article

Interface engineering of bifunctional electrocatalysts for hydrazine-assisted hydrogen production

Wenxin Wang[1], Yibing Liu[1], Syed Awais Ahmad[2], Jing Wang[1](✉), Ali auf[3](✉), Erjun Zhao[4](✉), Qingrui Zhang[1](✉), Faming Gao[5]

[1] State Key Laboratory of Metastable Materials Science and Technology, Hebei Key Laboratory of Heavy Metal Deep-Remediation in Water and Resource Reuse, Yanshan University, Qinhuangdao, Hebei 066004, China

[2] College of Physics and Electronics Information, Yunnan Key Laboratory of Opto-Electronic Information Technology, Key Laboratory of Advanced Technique & Preparation for Renewable Energy Materials-Ministry of Education, Yunnan Normal University, Kunming 650000, China

[3] Department of Chemistry and Chemical Engineering, Lahore University of Management Sciences (LUMS), Lahore 54792, Pakistan

[4] College of Science, Inner Mongolia University of Technology, Hohhot 010051, China

[5] School of Materials Science and Chemical Engineering, Tianjin University of Science and Technology, Tianjin 300457, China

Nano Res., **Just Accepted Manuscript** • https://doi.org/10.26599/NR.2026.94908709

https://www.sciopen.com/journal/1998-0124 on Apr. 3, 2026

TABLE OF CONTENTS (TOC)

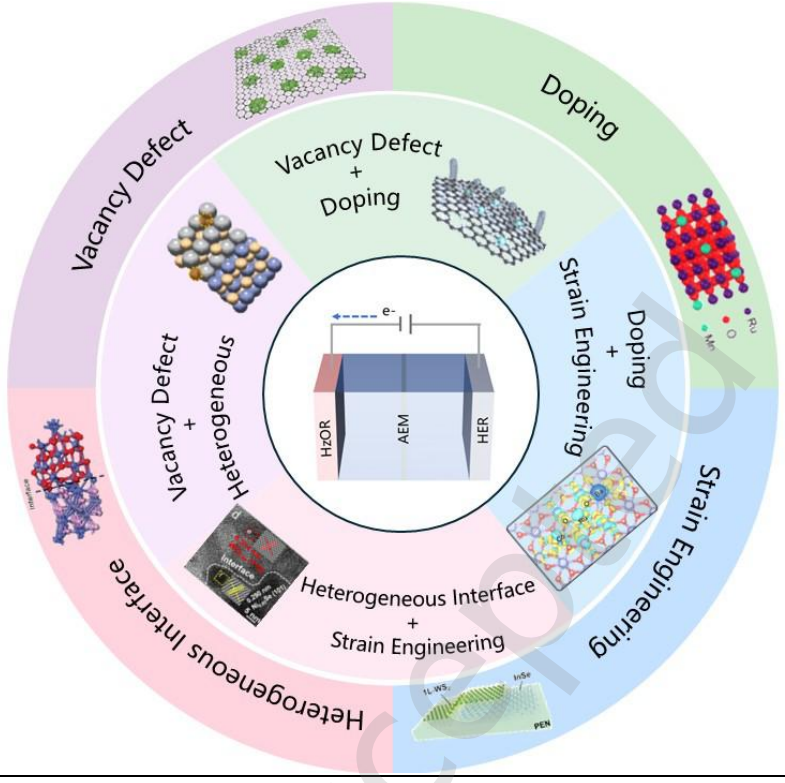

This review systematically summarizes interface regulation strategies for catalysts employed in hydrazine-assisted water splitting systems.

Nano Research

Open Access

Review Article

Interface engineering of bifunctional electrocatalysts for hydrazine-assisted hydrogen production

Wenxin Wang[1], Yibing Liu[1], Syed Awais Ahmad[2], Jing Wang[1]✉, Ali Rauf[3]✉, Erjun Zhao[4]✉, Qingrui Zhang[1]✉, and Faming Gao[5]

[1]*State Key Laboratory of Metastable Materials Science and Technology, Hebei Key Laboratory of Heavy Metal Deep-Remediation in Water and Resource Reuse, Yanshan University, Qinhuangdao, Hebei 066004, China*
[2]*College of Physics and Electronics Information, Yunnan Key Laboratory of Opto-Electronic Information Technology, Key Laboratory of Advanced Technique & Preparation for Renewable Energy Materials-Ministry of Education, Yunnan Normal University, Kunming 650000, China*
[3]*Department of Chemistry and Chemical Engineering, Lahore University of Management Sciences (LUMS), Lahore 54792, Pakistan*
[4]*College of Science, Inner Mongolia University of Technology, Hohhot 010051, China*
[5]*School of Materials Science and Chemical Engineering, Tianjin University of Science and Technology, Tianjin 300457, China*

Received: 7 March 2026; **Revised:** 31 March 2026; **Accepted:** 3 April 2026

✉Address correspondence to Jing Wang, jwang6027@ysu.edu.cn; Ali Rauf, Ali.Rauf@lums.edu.pk; Erjun Zhao, ejzhao@imut.edu.cn; Qingrui Zhang, zhangqr@ysu.edu.cn

Cite this article: *Nano Research*, 2026, 19, 94908709 https://doi.org/10.26599/NR.2026.94908709

ABSTRACT: Facing global energy and environmental challenges, hydrogen is seen as a crucial clean energy carrier. Conventional water electrolysis is hindered by the sluggish kinetics of the anodic oxygen evolution reaction (OER). Replacing OER with the hydrazine oxidation reaction (HzOR) offers a much lower theoretical potential (-0.33 V vs. RHE), faster kinetics, and the production of only N_2, eliminating explosion risks from H_2/O_2 mixtures. Achieving high-performance hydrazine-assisted water splitting requires advanced electrocatalysts that efficiently drive both the hydrogen evolution reaction (HER) at the cathode and HzOR at the anode. Interface engineering, constructing and modulating the interfaces between different material components, has emerged as a powerful strategy to optimize catalyst properties. By precisely designing interfaces, researchers can synergistically tune electronic structures, expose more active sites, facilitate charge transfer, and enhance stability. The review first outlines the fundamental mechanisms of HER and HzOR, introducing key descriptors like hydrogen adsorption free energy (ΔG_{*H}). It then discusses advanced characterization techniques essential for probing interfacial structures and *in situ/operando* methods. The core of the article focuses on major interfacial engineering strategies, which includes vacancy defects, doping, heterostructures, and strain engineering. Each strategy is illustrated with recent exemplary catalysts, demonstrating how interface design leads to superior HER/HzOR bifunctional activity, high current density at low cell voltages, and remarkable long-term durability. The review concludes by highlighting the progress made and future challenges in developing practical, high-performance catalysts for this energy-saving hydrogen production technology.

KEYWORDS: electrocatalysis, hydrazine oxidation, hydrogen production, interfacial engineering, synergistic effect

1 Introduction

The increasingly severe energy crisis and environmental pollution pose significant challenges to global sustainable development[1, 2]. Hydrogen energy is widely regarded as the "ultimate energy of the 21st century" due to its clean credentials[3, 4]. It has become a crucial pathway for China to promote energy structure transformation and achieve carbon neutrality goals[5-7]. Among various hydrogen production technologies, electrocatalytic water splitting has attracted considerable attention due to its high efficiency and energy-saving characteristics[8-10]. This process consists of two half-reactions, i.e., the hydrogen evolution reaction (HER) and the oxygen evolution reaction (OER). OER, involving a four-electron transfer process ($2H_2O \rightarrow O_2 + 4H^+ + 4e^-$), suffers from a high theoretical potential (+1.23 V vs. RHE) and sluggish reaction kinetics, which limit the overall efficiency of water splitting. To overcome the limitations of OER, researchers have recently focused on developing alternative oxidation reactions involving small molecules such as ethanol (0.059 V vs RHE)[11, 12], glucose (0.05 V vs RHE)[13], urea (0.37 V vs RHE)[14] and sulfide ions (0.142 V vs RHE)[15] , aiming to reduce the energy barrier and enhance reaction rates[16, 17]. Among these, the hydrazine oxidation reaction (HzOR, -0.33 V vs RHE) exhibits an extremely low theoretical potential and produces only N2 as the sole product, demonstrating significant advantages in potential and environmental friendliness[18-20]. The HzOR-assisted hydrogen production strategy stands out for its ability to realize efficient hydrogen generation. Unlike

conventional water electrolysis, it circumvents the safety risks caused by H_2/O_2 mixture formation. This advantage directly leads to a substantial enhancement in the overall safety of hydrogen production.

To achieve superior hydrazine-assisted water splitting performance under specific catalytic conditions, the development of well-designed electrocatalysts is essential[21-23]. An ideal catalyst should possess optimized physical and chemical properties to facilitate reactant adsorption and product desorption. As different components can serve as active centers for multiple reactions[24, 25], rational morphology control helps expose more active sites, thereby enhancing intrinsic activity[26-28]. Meanwhile, the electronic structure of the catalyst governs the electron transfer process and profoundly influences the formation of reaction intermediates and the desorption of final products[29-31]. Therefore, precise design and synergistic modulation of material composition, morphology, and electronic structure are key strategies for constructing high-performance electrocatalysts and achieving breakthrough performance. In this context, interfacial engineering has emerged as an effective approach[32-34]. Catalysts designed based on interfacial engineering typically comprise two or more components[35]. By rationally regulating atomic arrangements at the interface, the physical and chemical properties of electrocatalysts can be effectively tuned. Furthermore, the strong coupling interactions between distinct components, together with the engineered interfacial structure, boost electron conduction efficiency. At the same time, they markedly enhance structural stability throughout electrocatalytic reactions.

Over the past decades, a range of excellently interface-regulated catalysts has been extensively investigated. For instance, Wei et al. [36] systematically reviewed recent advances in interfacial engineering for efficient HER catalysts, and Song et al. [37] summarized interfacial engineering strategies in electrocatalytic heterogeneous catalysts. However, despite considerable progress in electrocatalyst research, comprehensive reviews on bifunctional catalysts for HzOR-assisted hydrogen production remain scarce. To meet the demands of future electrochemical energy conversion and storage, it is imperative to develop controllable optimization strategies for HER/HzOR bifunctional catalysts to synergistically enhance their energy density, power density, catalytic activity, efficiency, and durability.

This review provides a systematic overview of interface regulation strategies for catalysts in hydrazine-assisted water splitting systems. It begins with an introduction to the reaction mechanisms of HER and HzOR, followed by a focused discussion on various interfacial engineering strategies for bifunctional catalysts within this system, including vacancy defects, doping modulation, heterostructures, strain engineering, and single-atom catalysts. Finally, an outlook is provided on the remaining challenges and future development of HER/HzOR bifunctional catalysts and hydrazine-assisted water splitting technology.

You can simply type your text into this template or modify an already prepared manuscript based on the template formatting.

2. Mechanistic and theoretical of HER and HzOR

The overall reaction of HER (cathode) and HzOR (anode) in an alkaline medium is as follows:

Cathode: $4H_2O + 4e^- \rightarrow 2H_2 + 4OH^-$

Anode: $N_2H_4+4OH^-\rightarrow N_2+4H_2O+4e^-$

Overall reaction: $N_2H_4\rightarrow N_2+2H_2$

2.1 HER mechanism

In an acidic medium, the cathodic reaction is as follows:

Overall reaction: $2H^+ + 2e^- \rightarrow H_2$

Volmer reaction: $H^+ + e^- \rightarrow *H$

Tafel reaction: $*H + *H \rightarrow H_2$

Heyrovsky reaction: $H^+ + *H + e^- \rightarrow H_2$

In alkaline media, the cathodic reaction is as follows:

Overall reaction: $2H_2O + 2e^- \rightarrow H_2 + 2OH^-$

Volmer reaction: $H_2O + e^- \rightarrow *H + OH^-$

Tafel reaction: $*H + *H \rightarrow H_2$

Heyrovsky Reaction: $H_2O + e^- + *H \rightarrow H_2 + OH^-$

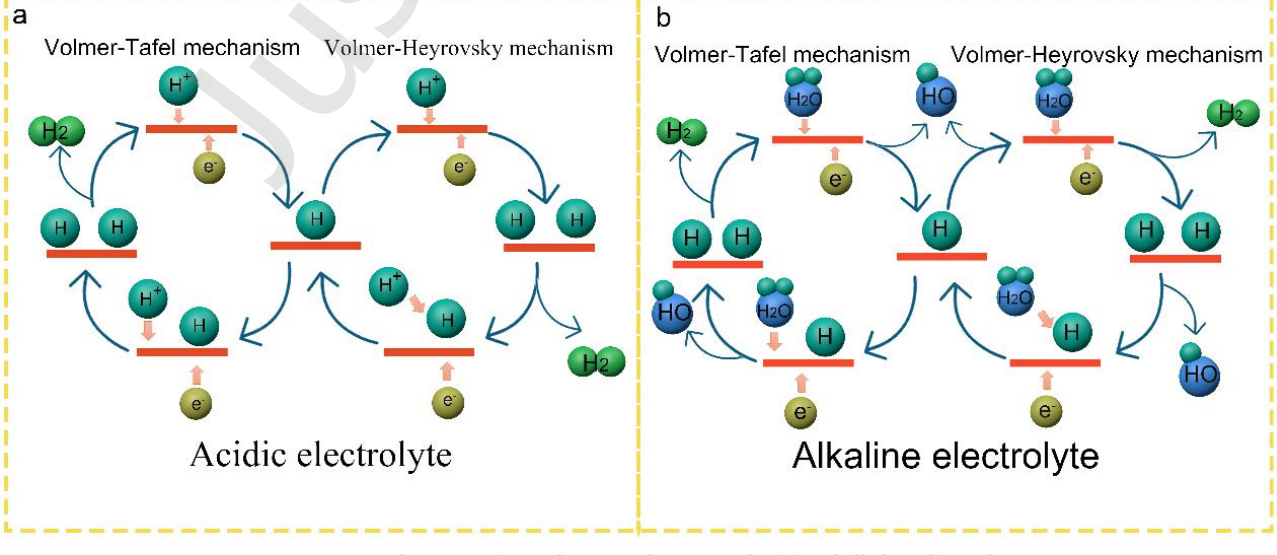

Figure 1. Mechanisms of HER electrocatalysis in acidic (a) and alkaline (b) media.

The HER can proceed via either the Volmer-Heyrovsky or Volmer-Tafel mechanism (as shown in Fig. 1). The first step is the Volmer reaction, which involves H_3O^+ in acidic media or H_2O in alkaline media to generate *H. The second step

serves as the rate-determining step (RDS), whose kinetics depend on the activity of the catalysts involved[38]. It has been widely reported in the literature that HER kinetics in alkaline conditions are significantly slower than those in acidic conditions[39-41]. In alkaline media, *H primarily originates from the water dissociation process, thereby significantly increasing the overpotential for the alkaline HER[42].

2.2 Volcano plot

According to the Sabatier principle, the adsorption strength between the catalyst surface and reactant molecules must be moderate[43]. If the adsorption is too weak, the reactants cannot be effectively activated; if it is too strong, the products struggle to desorb from the catalyst surface. Only when the adsorption strength is within an appropriate range can the catalytic reaction efficiency be maximized. The hydrogen adsorption free energy (ΔG_{*H}) serves as a key descriptor for evaluating the behavior of H adsorption and H_2 desorption in the HER[44]. The Sabatier principle indicates that under ideal conditions, ΔG_{*H} should approach zero, at which point the exchange current density (j_0) of the HER reaches its maximum.

The characteristic "volcano" relationship in the HER has been robustly confirmed by correlating experimental j_0 with the ΔG_{*H}, the latter being readily accessible through density functional theory (DFT) calculations. The peak of this volcano curve represents the optimal scenario where ΔG_{*H} is close to zero.[45] Deviations from this ideal value reduce the activity, as j_0 grows exponentially when ΔG_{*H} is too small but declines exponentially when overly strong hydrogen adsorption makes ΔG_{*H} excessively negative (Fig. 2(a)). The pioneering work of Nørskov et al. [46], who first constructed this curve using DFT, has established a standard framework now universally applied for calculating ΔG_{*H} and predicting catalyst activity[47-49], as visually summarized by the volcano plot in Fig. 2(b).

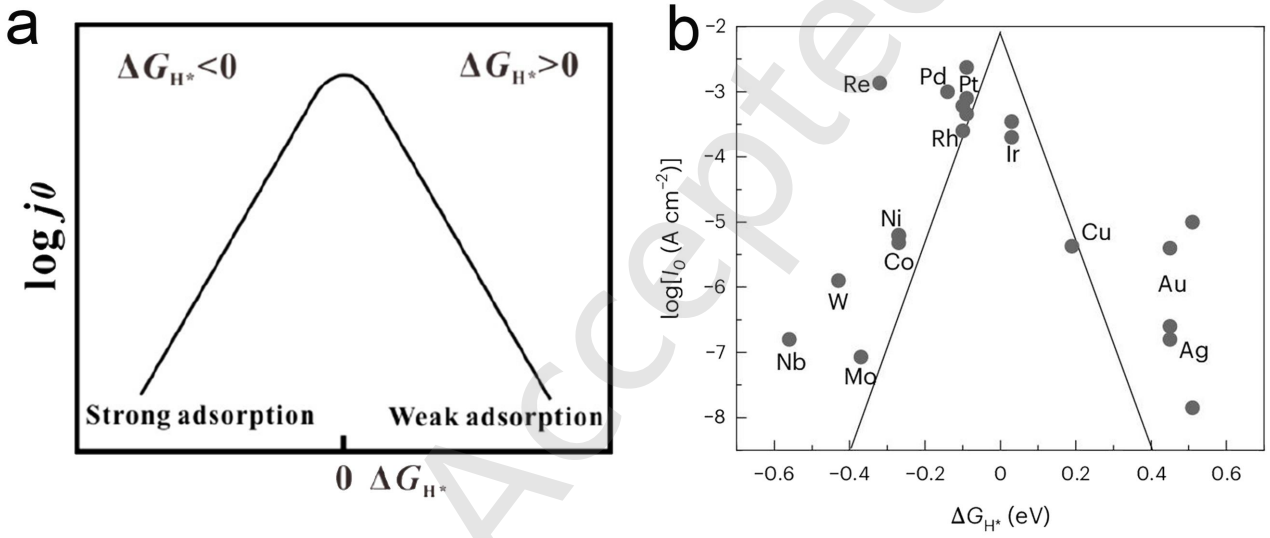

Figure 2. Volcano plot for HER. (a) Relationship between j_0 and ΔG_{*H} under the assumption of a Langmuir adsorption model. Reprinted with permission from Ref [45], © Royal Society of Chemistry 1958. (b) The dependence of j_0 on ΔG_{*H} for various materials. Reprinted with permission from Ref [47], © Springer Nature2025. The ΔG_{H^*} in the figure is consistent with the ΔG_{*H} in the text.

2.3 HzOR mechanism

The reaction mechanism of HzOR is considered to involve two pathways. As shown in Fig. 3(a), the stepwise dehydrogenation mechanism in HzOR begins with the chemical adsorption of N_2H_4 molecules on the electrode surface. Subsequently, OH^- ions in the electrolyte nucleophilic ally abstract protons from the N_2H_4 molecules, forming H_2O. After the stepwise cleavage of four N-H bonds, N_2 molecules are ultimately generated. Throughout this oxidation process, only N_2 is produced at the anode, without the formation of any by-products[50, 51].

$N_2H_4 \rightarrow *N_2H_4$

$*N_2H_4 \rightarrow *N_2H_3 + H^+ + e^-$

$*N_2H_3 \rightarrow *N_2H_2 + H^+ + e^-$

$*N_2H_2 \rightarrow *N_2H + H^+ + e^-$

$*N_2H \rightarrow *N_2 + H^+ + e^-$

$*N_2 \rightarrow * + N_2$

The other proposed reaction mechanism begins with the adsorption of N_2H_4 onto the catalytic active sites (Fig. 3(b)), followed by homolytic cleavage of the N-N bond, generating two $-NH_2$ radicals. Subsequently, these intermediates undergo a two-step H^+ abstraction by OH^-, ultimately forming N_2[18].

$N_2H_4 \rightarrow *N_2H_4$

$*N_2H_4 \rightarrow 2*NH_2$

$2*NH_2 \rightarrow 2*NH + 2H^+ + 2e^-$

$2*NH \rightarrow 2*N + 2H^+$

$2*N \rightarrow N_2$

Based on existing research, the RDS of the HzOR is generally the dehydrogenation process of the intermediate species $*N_2H_x$ (x = 1, 2, 3). The specific location of the rate-determining step may vary slightly among different catalyst systems, but it predominantly revolves around the dehydrogenation of these intermediates[16].

In alkaline media, the HER is limited by the sluggish Volmer step (water dissociation), while the HzOR efficiency is determined by the dehydrogenation kinetics of N_2H_x intermediates. Both reactions require catalysts with optimized adsorption energetics. These prerequisites make interfacial engineering an essential strategy, as it enables precise modulation of electronic structures, construction of synergistic active sites, and stabilization of reaction intermediates.

3. Structural characterization of interfaces

3.1 Transmission electron microscope

As a powerful and widely used characterization technique, transmission electron microscope (TEM) provides atomic-scale visualization of electron-transparent specimens. Its operation relies on the interaction between a high-energy electron beam with the sample[52]. The resulting image contrast arises from specific electron-sample interactions and can be leveraged to extract interfacial information in polycrystalline materials. When combined with electron diffraction and spectroscopic methods, TEM offers multiple imaging modes capable of resolving phase structure and chemical composition with ultrahigh spatial resolution (<1 Å)[53]. In particular, for interface structures with varying crystallographic orientations, high resolution TEM (HRTEM) provides direct evidence for structural identification. For example, the group of Yang proposed a strategy based on positively charged Ru-N-Ni dual sites[54]. As shown in Fig. 4(a), HRTEM images display two distinct sets of lattice fringes corresponding to Ru and Ni_3N, indicating a well-defined interface between Ru nanoparticles and Ni_3N nanosheets. Inverse fast Fourier transform analysis of the selected region in Fig. 4(a) further verifies the presence of Ru nanoparticles, revealing coherent lattice fringes from both phases. In another study, Wang et al. [55] synthesized a cobalt-vanadium bimetallic catalyst via a liquid-phase self-assembly strategy. This approach successfully modulated the electronic structure of the catalyst. As a result, the HER and OER performances were significantly enhanced. The HRTEM image (Fig. 4(b)) clearly shows distinct lattice fringes and intimate contact between $Co_2N_{0.67}$ (101) and VN (200). This observation confirms the formation of a heterojunction.

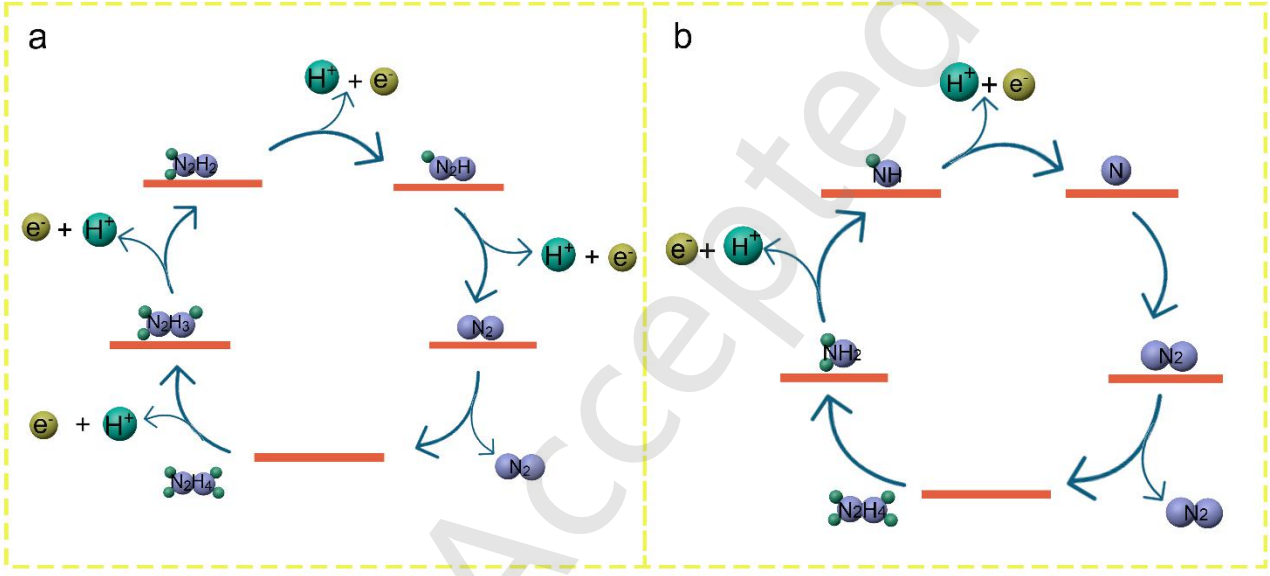

Figure 3. Schematic of the HzOR pathway.

3.2 High-angle annular dark-field scanning transmission electron microscopy

High-angle annular dark-field scanning transmission electron microscopy (HAADF-STEM) is highly sensitive to the atomic number (Z) of elements in a specimen. By collecting electrons scattered to large angles with an annular detector, it produces Z-contrast images whose intensity is approximately proportional to Z^2 along the electron-beam path. Consequently, heavier atoms appear brighter than lighter ones, enabling direct visualization of interfacial structures[56]. For example, Yan et al. [57] used a co-electrodeposition strategy to introduce iridium single atoms into ultrathin, porous $NiCo_2O_4$ nanosheets. HAADF-STEM analysis confirmed the structural configuration of the synthesized Ir-$NiCo_2O_4$ nanosheets, in which the $NiCo_2O_4$ lattice was oriented along the [111] direction (Fig. 4(c)). Furthermore, aberration-corrected HAADF-STEM enabled direct resolution of the spatial distribution of Ir species. High-resolution images revealed numerous bright, spot-like features (Fig. 4(d)), which provide clear evidence for the atomic-scale isolation of Ir sites within the nanosheet matrix. It is seen that the HAADF-STEM is particularly powerful for identifying individual atoms and resolving atomic-scale interfacial configurations, especially in single-atom catalysts.

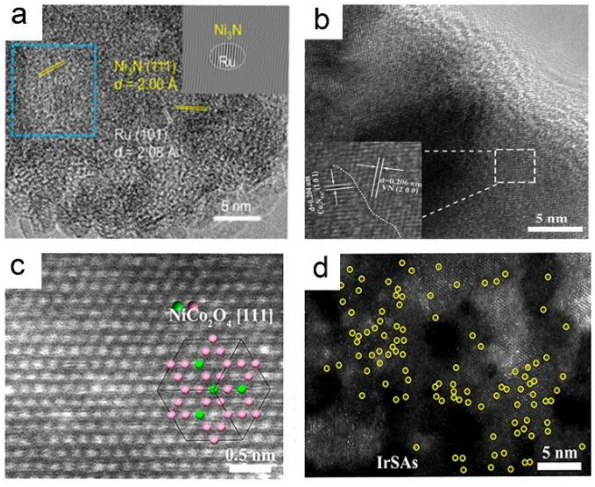

Figure 4. TEM and HAADF-STEM image. (a) HRTEM image (inset is the inverse Fourier transform corresponding to the blue box). Reprinted with permission from Ref [54], © John Wiley and Sons 2025. (b) HRTEM image of $Co_2N_{0.67}$ and VN. Reprinted with permission from Ref [55], © John Wiley and Sons 2024. (c) HAADF-STEM image of Ir-$NiCo_2O_4$ NSs. The insert in (c) show the corresponding crystal structure of $NiCo_2O_4$ unit cells taken along the [111] orientation. (d) the HAADF-STEM image of Ir-$NiCo_2O_4$ NSs, indicating the Ir-SAs. Reprinted with permission from Ref [57], © American Chemical Society 2020.

3.3 X-ray photoelectron spectroscopy

X-ray photoelectron spectroscopy (XPS) is a surface-sensitive technique that detects photoelectrons emitted from the top few nanometers of a material, and it is widely used to investigate surface chemical composition and elemental valence states. It is a surface-sensitive, non-destructive technique that provides direct evidence of charge transfer between different components. Hui et al. [58] developed a strain-engineered Rh single-atom catalyst anchored on a carbon nanotube-supported curved WS_2 substrate (Rh_{SA}/WS_2@CNT) to modulate the electronic structure. The XPS analysis of the S 2p and Rh 3d core-level signals is shown in Fig. 5(a,b). The Rh 3d spectrum exhibits two distinct spin-orbit split peaks at 308.48 eV and 313.17 eV. The Rh $3d_{3/2}$ peak is broader than the Rh $3d_{5/2}$ peak due to the Coster-Kronig effect. This indicates the successful incorporation of Rh single atoms into the WS_2@CNT support. Notably, the introduction of Rh causes a downshift in the binding energy of both the S 2p (Fig. 5(a)) and W 4f peaks. This suggests electron transfer from Rh to WS_2 and the partial oxidation of Rh. Pang et al. [59] fabricated a Fe_2O_3 nanotube substrate via a hydrothermal method. Subsequently, NiCo-LDH nanosheets were epitaxially grown on this substrate, followed by the loading of MoS_2 quantum dots and a low-temperature phosphidation treatment, ultimately yielding a stable heterostructure. The XPS spectra in Fig. 5(c-e) reveal the presence of both M-P and M-O (M = Ni, Co) bonds in FeP@NiCoP/Mo_4P_3. The M-O features originate from slight surface oxidation of metal atoms. Compared to the precursor, the Fe, Co, and Ni 2p peaks shift negatively after phosphidation. This confirms electron transfer from P to metal via strong covalent M–P bonds, which increases the electron density at metal sites and activates catalytic centers. In Fig. 5(f), the Mo 3d spectrum shows peaks at 228.1 and 231.7 eV, corresponding to $Mo^{\delta+}$ species. These results demonstrate the utility of XPS in probing interfacial electron redistribution and active-site regulation induced by phosphidation.

3.4 X-ray absorption spectroscopy

X-ray absorption spectroscopy (XAS) is widely used to probe the local geometric and electronic structures of selected elements by recording the energy-dependent fine structure of the element-specific absorption coefficient. When the incident photon energy is sufficient to excite core electrons into unoccupied states, strong absorption occurs and a sharp absorption edge appears[60]. The shape of the absorption edge is sensitive to the oxidation state and electronic structure of the probed element. The oscillations in the XAS spectrum beyond the absorption edge arise from the interference between the outgoing and backscattered photoelectron waves, reflecting the local atomic structure[37]. A key advantage of XAS lies in its element-specific sensitivity, enabling the characterization of local coordination environments even for amorphous or highly dispersed interfacial species. Owing to its sensitivity to the chemical state, local symmetry, and chemical bonding of the absorbing atom, XAS provides information about the spatial arrangement of its nearest neighbors. Interfacial architectures can therefore be inferred by identifying heteroatomic bonds that bridge distinct components For instance, X-ray absorption near-edge structure (XANES) fingerprints oxidation state and ligand environment, while extended X-ray absorption fine structure (EXAFS) can fully depict structural symmetry, coordination information, and bond lengths.

Recently, Zheng et al. [61] proposed a synergistic strategy that constructs active microregions through vacancies and doped. Synchrotron-based XAS together with DFT elucidated the atomic-scale electron-regulation mechanism. Ru K-edge XANES places Ru in a mixed valence state between 0 and +4 (Fig. 5(g, h)). Quantitative EXAFS fitting revealed a Ru-O-Mo coordination configuration, and its wavelet transform analysis ruled out Ru-Ru contributions, corroborating the atomic dispersion of Ru. Fig. 5(i) shows that the Mo K-edge XANES spectra indicates electron state delocalization in Mo induced by Ru doping. This reconstruction triggers electron transfer within the Mo-O-Ru structure and reorganizes the coordination microenvironment of low-crystalline MoO_{3-x}. DFT further revealed that the Ru-O-Mo distance (3.57 Å) is shorter than the original Mo-O-Mo distance (3.63 Å), forming a more compact short-bond network and markedly increasing the electron density on O atoms (Bader charge up to 1.03 |e|).

3.5 *In suit/operando* characterizations

To acquire authentic interfacial structural information under realistic electrocatalytic conditions, real-time characterization *in situ/operando* techniques is crucial, which reveal the dynamic evolution of reaction intermediates under actual working conditions.

3.5.1 In situ Raman spectroscopy

In situ Raman spectroscopy monitors changes in the vibrational frequencies of interfacial chemical bonds, thereby inferring dynamic processes such as interface formation and electronic structure evolution during reactions. Li et al.[62] investigated the effect of Ru doping on surface species evolution of the NiP_2 catalyst using in situ Raman spectroscopy. As shown in Fig. 4(a, c), in 1 M KOH without urea, the Raman characteristic peaks of NiOOH (473/553 cm^{-1}) appeared for NiP_2 at 1.60 V. In contrast, for NiP2-Ru, these signals emerged at a lower potential of 1.55 V. This indicates that Ru doping effectively lowers the formation potential of NiOOH where by the Ni^{3+} is the active site. Further in situ Raman spectroscopy analysis in an electrolyte containing urea gives rise to similar trend (Fig. 4(b, d)). For NiP_2, NiOOH signals were not detected even when the potential was increased to 1.65 V. On the contrary, the NiOOH peak is remained for NiP_2-Ru, although the internsity is silightly reduced. It is seen that the in situ Raman results provide direct evidence the reveal the reaction mechnism. Similarly, Wang et al. [63] also employed *in situ* Raman spectroscopy to demonstrate the formation of NiOOH. As shown in Fig. 6(e), during OER measurements, changes in the peak positions were observed as the potential increased from 1.1 V to 1.6 V. At 1.1 V, two peaks attributed to the $Ni(OH)_2$ phase were observed at 450 cm^{-1} and 519 cm^{-1}. When the potential increased to 1.3 V, these peaks gradually shifted to positions at 464 cm^{-1} and 545 cm^{-1}, corresponding to the E_g bending vibration and A_{1g} stretching vibration of the Ni-O bond in the NiOOH phase, respectively. This finding indicates that at potentials above 1.2 V, the dehydrogenation step of lattice hydroxyl groups occurs,

generating the active NiOOH phase.

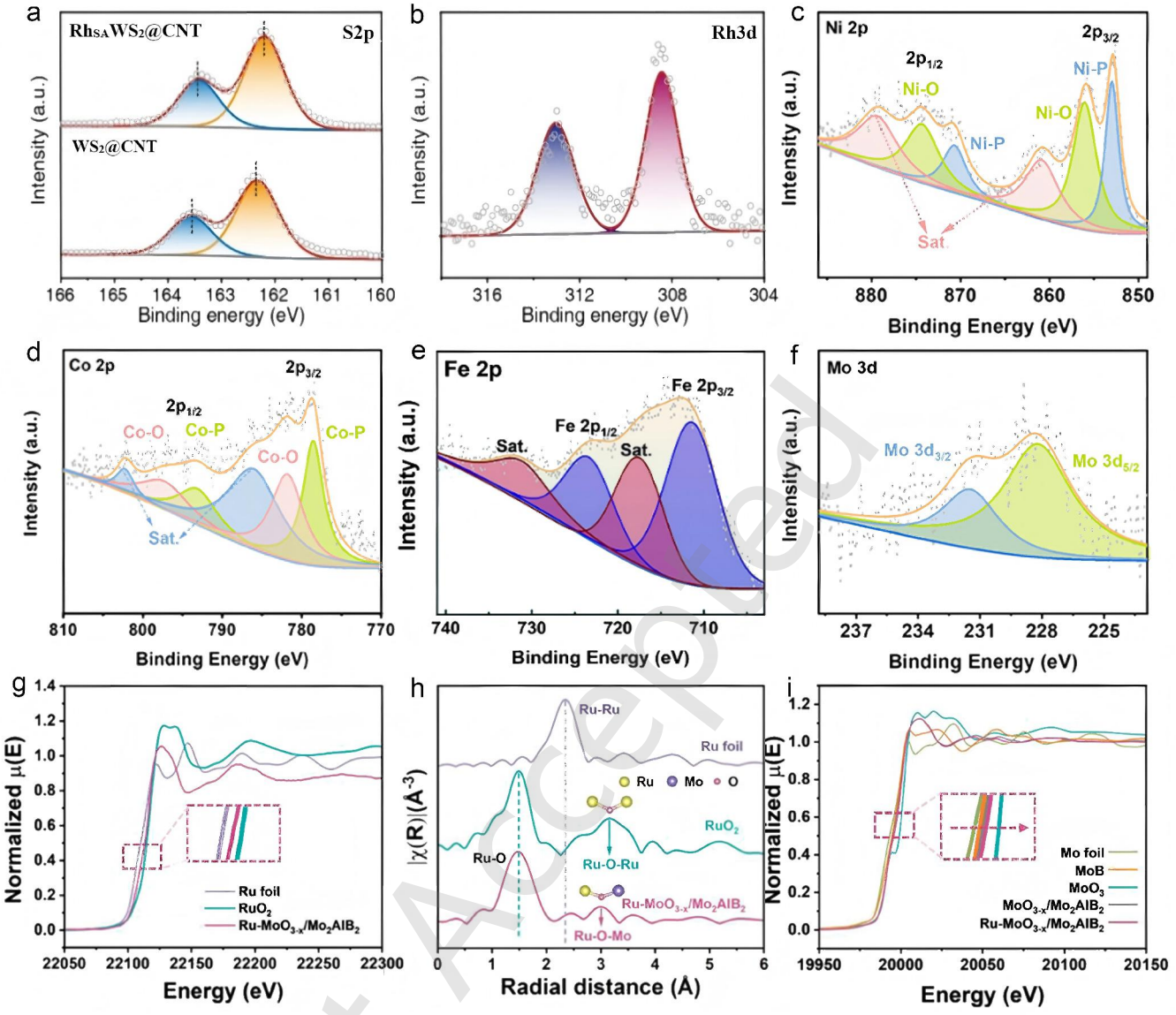

Figure 5. XPS and XAS spectra. High-resolution XPS spectra of (a) S 2p, (b) Rh 3d. Reprinted with permission from Ref [58], © American Chemical Society 2025. High-resolution XPS spectra of (c) Ni 2p, (d) Co 2p, (e) Fe 2p, (f) Mo 3d. Reprinted with permission from Ref [59], © John Wiley and Sons 2025. (g) Ru K-edge XANES. (h) Ru K-edge FT-EXAFS. (i) Mo K-edge XANES. Reprinted with permission from Ref [61], © John Wiley and Sons 2025.

3.5.2 In situ X-ray absorption spectroscopy

In situ X-ray absorption spectroscopy (XAS) is a powerful technique for probing the local atomic structure of catalytic sites under operating conditions, thereby enabling the identification of true active centers in electrocatalysts. Yuan et al. [64] performed potential-dependent *in situ* XAFS measurements to investigate the dynamic evolution of atomically dispersed Se sites during HzOR. The XANES spectra (Fig. 6(f)) and the derived energy shift (ΔE) plot (Fig. 6(g)) reveal a stepwise increase in the Se oxidation state upon shifting to open-circuit potential (ΔE = 1.4 eV) and a further slight increase during the electrochemical reaction (ΔE = 0.2 eV). These observations indicate that the Se catalytic sites differ in three environments, namely in air or water, at open circuit, and during the reaction. After the reaction, the oxidation state of Se returns to the open-circuit state, which demonstrates the structural stability and reproducibility of atomically dispersed Se sites during the HzOR. To further clarify the evolution of the local atomic coordination environment of the Se catalytic centers under the three conditions, the k^3-weighted Fourier-transformed EXAFS spectra were compared (Fig. 6(h)). Under air and water conditions, the main peak corresponding to Se-C/N/O is almost identical, located at 1.56 Å, which is larger than the main peak (1.47 Å) observed at open circuit and during the reaction. This change indicates that the local atomic coordination environment of the Se sites has undergone a certain degree of alteration to match the bond lengths. A least-squares EXAFS curve-fitting analysis was performed to evaluate the three backscattering pathways of Se-C, Se-O, and Se-N (Fig. 6(i)). Under air and water conditions, the bond length is 1.88 Å with four Se-C coordination, corresponding to the original state of the SeC_4 sites. These combined observations (Fig. 6(f-i)) provide direct evidence for the reversible changes in both oxidation state and local coordination environment of the Se active sites under operating conditions.

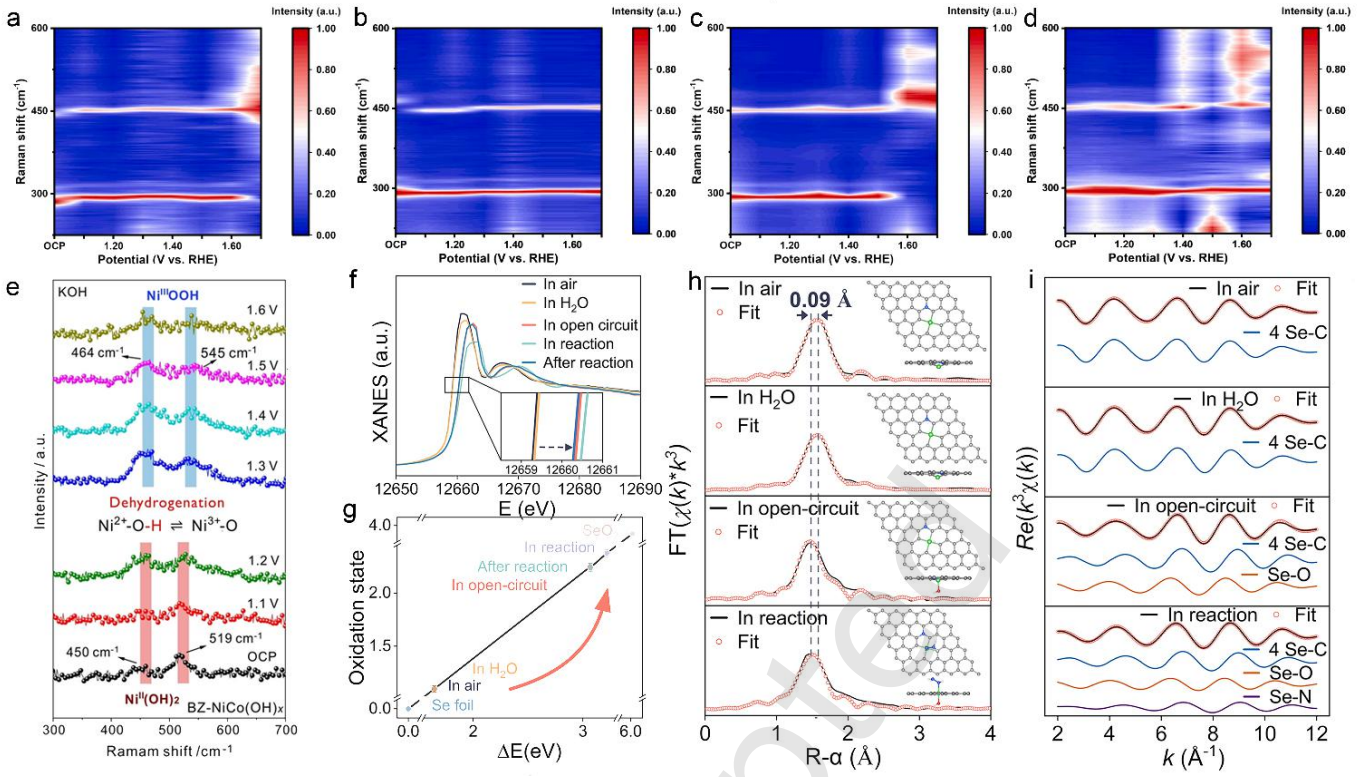

Figure 6. *In situ* Raman and XAS spectra. Raman spectra of NiP_2 in (a) 1 M KOH and (b) 1 M KOH with 0.33 M urea. (c) Raman spectra of NiP_2-Ru in 1 M KOH and (d) 1 M KOH with 0.33 M urea. Each potential increment was 0.05 V when the potential was varied from the open-circuit potential to 1.70 V. Reprinted with permission from Ref [62], © Elsevier 2025. (e) *In situ* Raman detection of BZ-NiCo(OH)$_x$ for OER in 1 M KOH electrolyte without HMF. Reprinted with permission from Ref [63], © John Wiley and Sons 2024. (f) Se K-edge XANES spectra of Se@C-1000 under different conditions. (g) The fitted average oxidation states of Se from XANES spectra; data are represented as mean ± SEM. First-shell fitting of EXAFS spectra (h) and corresponding Re (k^3 χ(k)) oscillations of different fitting paths for the sample under different conditions (i). Inset in (h), corresponding geometric configurations. H, white; C, gray; N, blue; O, red; Se, green. Reprinted with permission from Ref [64], © Elsevier 2024.

4. Interfacial engineering strategies

Based on the intrinsic reaction mechanisms of HER/HzOR (Section 2), this section systematically elucidates interface engineering strategies for optimizing the bifunctional performance of electrocatalysts for hydrazine-assisted water splitting. These strategies include vacancy defect engineering, doping modulation, heterostructure construction, strain engineering, and single-atom catalyst design. Through these distinct structural engineering approaches, synergistic regulation of the interfacial electronic structure, intrinsic activity of active sites, and adsorption behavior of intermediates is achieved.

4.1 Vacancy defect

Vacancy defects can effectively modulate the surface electronic structure of catalysts, increasing the number of active sites, reducing the electron diffusion barrier, and narrowing the band gap, thereby enhancing the catalytic performance[65, 66]. Introducing vacancies into catalysts, characterized by the absence of atoms at specific lattice sites, serves as an effective strategy for fine-tuning the electronic structure[67]. Depending on the charge characteristics, vacancies can be classified into anion vacancies and cation vacancies.

4.1.1 Anion vacancy

Anionic vacancies (such as oxygen, phosphorus, sulfur, and selenium vacancies) are typically introduced via methods including chemical reduction using agents like $NaBH_4$, H_2, NH_3, or Al, as well as plasma etching[68-72]. Among these, oxygen vacancies, referring to the absence of oxygen atoms in the crystal lattice, are usually generated during synthesis under specific conditions such as temperature and atmosphere[73-75]. A representative study by Wang et al, [76] synthesized a bimetallic phthalate-based MOF rich in vanadium-oxygen vacancies ($NiIr_{0.03}$-BDC) as a model system to elucidate the underlying catalytic mechanism. *In situ* characterization results indicated that during the HzOR, the environment rich in oxygen vacancies facilitates the adsorption of OH^- on the catalyst surface, leading to the formation of active Ni(OH)$_x$ species (Fig. 7(a, b)). Furthermore, Fig. 7(c, d) shown that the introduced Ir enhances the HzOR activity of Ni sites by modulating their electronic structure. It also serves as an active HER site, given its favorable adsorption properties for *H_2O and *H intermediates.

Introducing controlled phosphorus vacancies into phosphide-based electrocatalysts is an established and effective strategy for boosting electrochemical performance[77, 78]. The group of Huang synthesized a CoH-CoPv@CFP material with P vacancies on carbon fiber paper using a $NaBH_4$ reduction method[79]. As shown in Fig. 7(e), the hydrogen adsorption free energy was calculated to be 1.85 eV for $Co(OH)_2$, indicating that the binding strength of H on its surface is too weak. For CoP, the ΔG_{*H} at the P site was 0.37 eV, which is lower than that of $Co(OH)_2$. After introducing P vacancies into CoP, the primary adsorption site in CoPv shifted to the Co atoms, and the corresponding ΔG_{*H} increased to 0.02 eV, approaching the thermoneutral

value of 0 eV. This modulation of the active site and adsorption energetics underpins the enhanced hydrogen evolution activity. Similarly, the group of Wang prepared a molybdenum-doped Ni_2P nanosheet array catalyst rich in P vacancies on a Mo-Ni foam substrate (Mo-Ni_2P_V@MNF)[80]. This catalyst served as a bifunctional electrocatalyst for overall hydrazine splitting in a seawater environment. It achieved an industrial-level current density of 1000 mA cm^{-2} with an ultralow cell voltage of only 571 mV and demonstrated exceptional stability, maintaining operation for over 1000 h (Fig. 7(f)). These studies collectively demonstrate how the engineering of P vacancies can effectively optimize intermediate adsorption and boost both activity and stability in electrocatalytic systems.

Selenium vacancies create favorable chemisorption sites for small molecules and their reaction intermediates. This characteristic positions them as potential active centers[81]. Due to their significant impact on electrocatalytic performance, this area has attracted growing research interest, with numerous important findings being reported[82, 83]. Yan et al. [84] fabricated a MoP/$MoSe_2$-H heterojunction rich in dual vacancies of P and Se as a hydrogen evolution catalyst. This structure provides abundant electrochemical active sites and exhibits excellent charge transfer capability. It significantly enhances the HER performance. In a 1 M KOH electrolyte, the catalyst demonstrates performance that approaches or even surpasses that of commercial Pt/C.

4.1.2 Cation vacancy

Regarding the fabrication of cation single-defect materials, the team led by Academician Xie Yi successfully introduced cation vacancies by selectively etching the alkali-soluble aluminum species from NiAl-LDH during nucleation and aging, utilizing an intra-layer Ostwald ripening process. These cation vacancies play a pivotal role in increasing the number of active sites, facilitating charge transfer, and enhancing gas diffusion[85]. Cation vacancies possess diverse electronic and

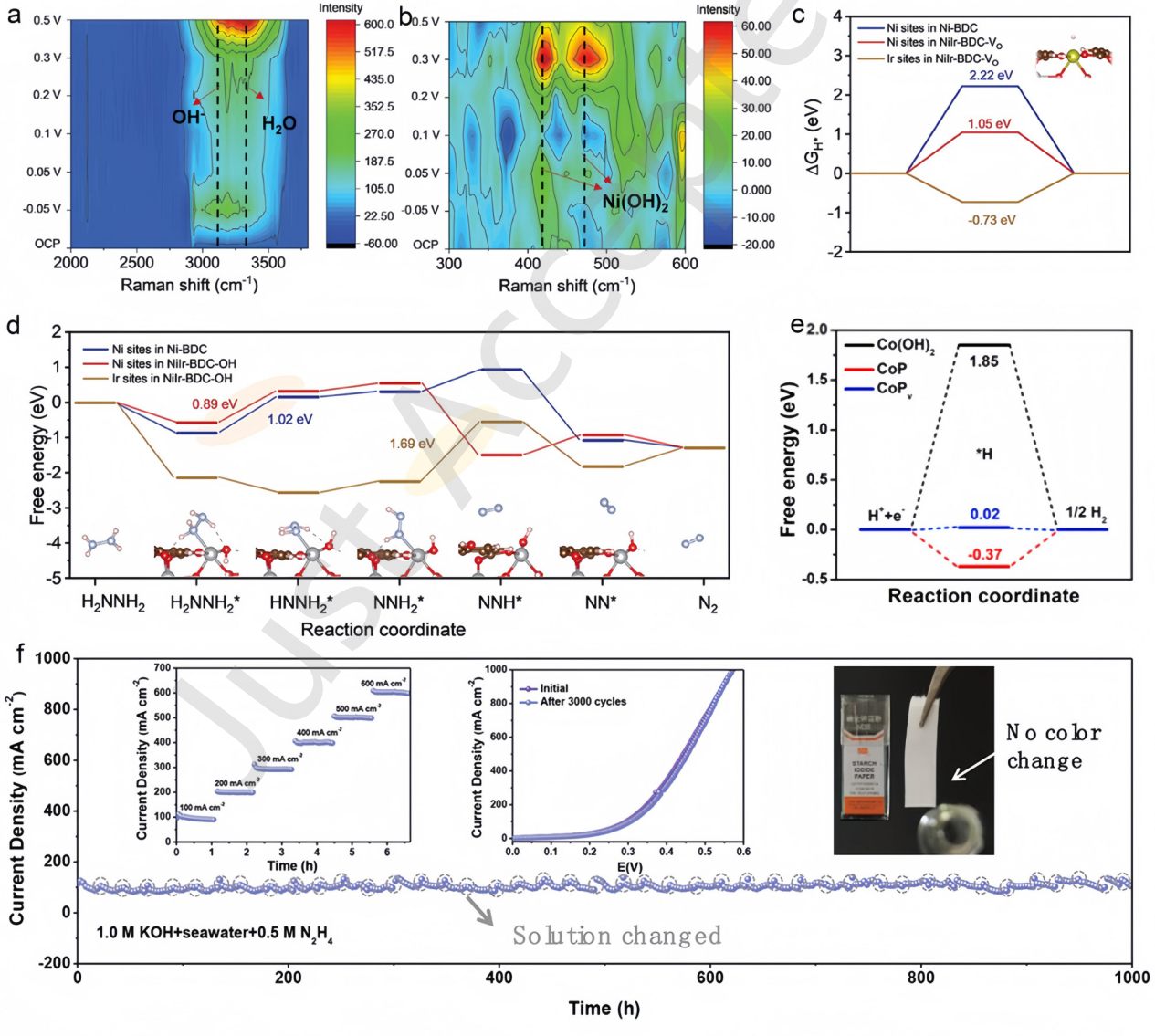

Figure 7. Vacancy engineering for hydrazine-assisted hydrogen production. (a, b) *In situ* Raman spectra of the $NiIr_{0.03}$-BDC at different applied potentials. (c) Free energy profiles of Ni-BDC (Ni sites), NiIr-BDC-V_O (Ni sites), and NiIr-BDC-V_O (Ir sites) for HER at equilibrium potential. (d) Free energy profiles of Ni-BDC (Ni sites), NiIr-BDC-OH (Ni sites), and NiIr-BDC-OH (Ir sites) for HzOR. Reprinted with permission from Ref [76], © John Wiley and Sons 2024. (e) Free energy diagram for *H adsorption on $Co(OH)_2$, CoP and CoP_V. Reprinted with permission from Ref [79], © Elsevier 2024. (f) Chronoamperometry i-t curve of the Mo-Ni_2P_V@MNF couple in 1.0 M KOH + seawater + 0.5 M N_2H_4 for 1000 h (Left inset shows the multi-current electrochemical process of Mo-Ni_2P_V@MNF; middle inset shows the polarization curves for Mo-Ni_2P_V@MNF before and after 3000 CV cycles; and right inset shows the image of the potassium iodide starch paper immersed in the electrolyte after 1000 h i–t test). Reprinted with permission from Ref [80],

orbital distributions[86]. They can effectively modulate the surface electronic structure. Moreover, they raise the valence state of adjacent metal centers[87]. As a result, the electrocatalytic activity is significantly enhanced[88-90]. As a representative example, Wang et al. [91] prepared a defect-rich cobalt catalyst supported on carbon cloth (D Co/CC), which maintained a high density of surface defects even after oxidation. It was observed that these defects facilitated rapid redox cycling between Co(II) and hydrazine, enabling the continuous regeneration of highly active Co(0) sites. DFT calculations further indicated that the introduced defects reduced the energy barrier for the chemical reduction of Co(II) by hydrazine. Additionally, the defects were found to enhance the intrinsic activity of the Co(0) sites in the direct reaction pathway.

4.2 Doping

The primary objective of doping is to modulate the local coordination environment and electronic structure of the catalyst by leveraging the unique properties of dopant atoms, thereby optimizing the adsorption/desorption energy barriers of reaction intermediates and enhancing the catalytic activity[92]. Furthermore, the doping process triggers partial atomic substitution in the host material. Through this substitution, the electronic structure of the material is precisely tailored[93]. Meanwhile, the transport and diffusion of charge carriers across the electrochemical double layer are promoted. These effects collectively enhance the catalyst surface's adsorption capacity for reactive species.

4.2.1 Anion doping

The introduction of anionic dopants (*e.g.*, S, N, P) into catalysts can leverage the synergistic effects between the dopant anions and host elements, inducing defect formation in the precursor matrix and facilitating the creation of active sites[94]. Notably, anionic dopants with high electronegativity exert a more profound influence on the electronic structure, which can modulate the adsorption/desorption energetics of reaction intermediates and even alter the reaction pathway selectivity[95]. For instance, Wang et al. [96] modulated the basal plane activity of $NiPS_3$ via non-metal heteroatom doping. Theoretical calculations confirmed that the valence-band filling degree of $NiPS_3$ governs both its intrinsic conductivity and hydrogen adsorption strength. Experimentally, carbon-doped $NiPS_3$ showed optimal HER activity due to its moderate valence-band filling (Fig. 8(a)). The carbon-nitrogen co-doped sample achieved near-Pt activity, requiring only 53.2 mV overpotential at 10 mA cm^{-2} in 1 M KOH (Fig. 8(b)) with a high exchange current density of 0.7 mA cm^{-2} (Fig. 8(c)).

4.2.2 Cation doping

Cationic doping serves as an effective strategy for modulating the electronic structure, crystal lattice, and chemical microenvironment of host materials by incorporating extrinsic cations (e.g., metal ions like Li^+, Na^+, Mg^{2+}, Al^{3+}, or non-metal ions like H^+). This approach enables precise optimization of the material's physical, chemical, and electrochemical properties via electronic interactions and lattice strain induced by dopants[97]. In electrocatalysis, cationic doping primarily enhances intrinsic activity by tuning the adsorption energy of reaction intermediates. For example, Co-doped MoS_2 exhibits a hydrogen adsorption ΔG_{*H} as low as 0.09 eV, which closely approaches the theoretical optimum[98]. In another case, a bifunctional Mo, Fe-Ni_3S_2 nanoarray catalyst synthesized via Fe and Mo co-doping retains its intrinsic active sites while the doping process creates a larger specific surface area and abundant high-index facets. This approach realizes the thorough exposure of active sites alongside the promotion of fast mass transport of reactants and products. The MoS_2 material prepared by the group of Zhang simultaneously incorporates Co doping, defect engineering, low crystallinity, and increased exposure of edge sites[99]. Through DFT calculations, the authors conducted a systematic investigation into the impact of Co doping on the intrinsic HER activity of MoS_2 (Fig. 8(d, e)). Undoped MoS_2 displays a broad bandgap of 1.396 eV, which is indicative of its typical semiconductor properties. Following the incorporation of Co atoms into the basal plane of MoS_2, the bandgap is drastically reduced to 0.147 eV, a change that points to a marked improvement in electronic conductivity. Doping Co at the edge sites gives rise to additional charge carriers, also suggesting robust charge interactions at the edges. Since Co has more d-orbital electrons than Mo, this results in an increase in occupied states within the valence band of Co-doped MoS_2. Adsorption energy calculations (Fig. 8(f)) show edge Co sites have a ΔG_{*H} value of -0.04 eV, likely arising from strong charge transfer between Co and adjacent S/Mo sites. Importantly, this value is even lower than that of the Pt (111) surface.

4.2.3 Dual doping of cations and anions

Anionic-cationic co-doping is an effective strategy that leverages the synergistic effects between simultaneously introduced cationic and anionic dopants to optimize the electronic structure and physicochemical properties of materials. It has been reported that Ce and N co-doped ReS_2 nanosheets (Ce, N-ReS_2) were successfully constructed via a hydrothermal method as an efficient electrocatalyst[100]. The co-doping of Ce and N synergistically modulates the electronic structure of ReS_2, significantly reducing the energy barrier for the water dissociation step in the water-splitting process. This work provides a novel electronic-structure-tuning strategy for designing high-performance water electrolysis catalysts.

Furthermore, Peng et al. [101] reported a dual-site catalyst in which S-stabilized Pt clusters and Ni-N_4 sites were co-anchored on a nitrogen-doped carbon support (denoted as Pt_n-S/Ni_1-NC). This catalyst exhibits outstanding activity for both HER and HzOR. When assembled into an overall hydrazine-splitting (OHzS) electrolyzer using a 1.0 M KOH /

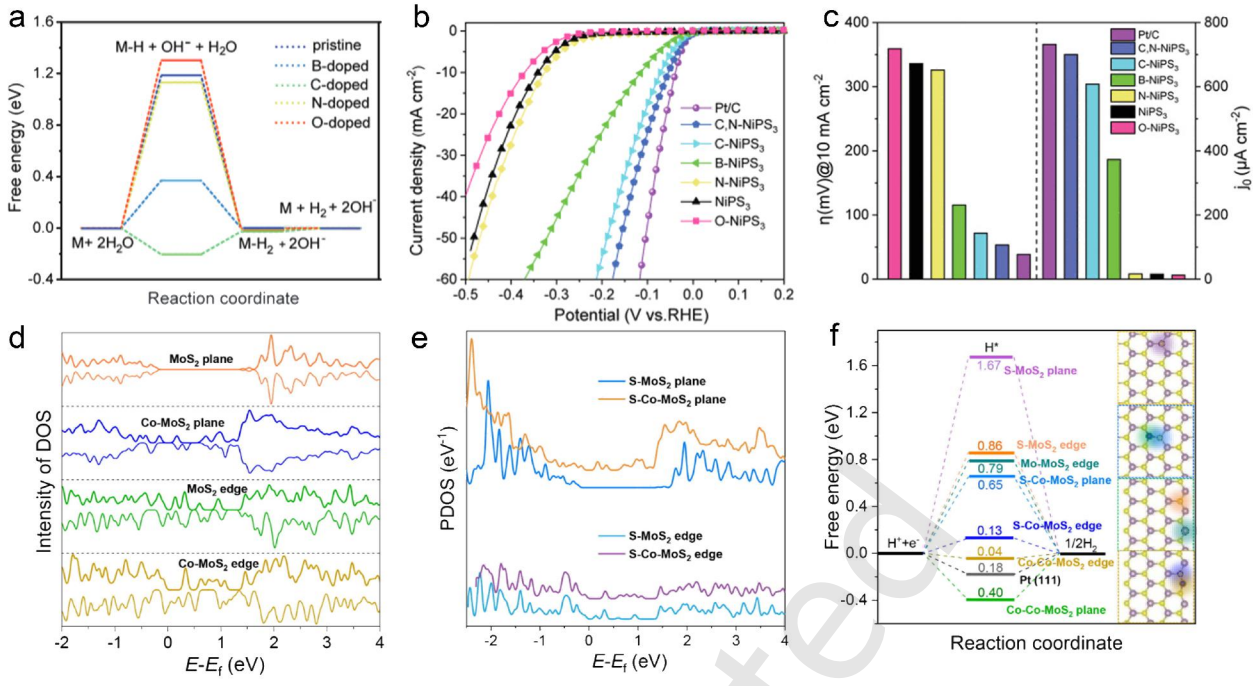

Figure 8. Anion and cation doping engineering for hydrazine-assisted hydrogen production. (a) Free energy diagram by the Volmer-Heyrovsky mechanism under steady-state H coverage on different catalysts. H coverage is defined by H occupation rate on congeneric sites (denoted as S-top sites), i.e., by the number of adsorbed H atoms on specific sites divided by the number of all congeneric sites. (b) LSV curves measured in 1 M KOH. (c) Summary of the overpotential at 10 mA cm^{-2} and exchange current density. Reprinted with permission from Ref [96], © John Wiley and Sons 2020. (d) DOS plots for MoS_2 plane, Co-MoS_2 plane, MoS_2 edge, and Co-MoS_2 edge. (e) PDOS of S sites at MoS_2 plane, Co-MoS_2 plane, MoS_2 edge and Co-MoS_2 edge. (f) Free energy corresponding to the reaction coordinates of different active sites. For comparison, the data of precious Pt (111) are also presented, insets show the atomic structures of the concerned sites. Reprinted with permission from Ref [99], © John Wiley and Sons 2022.

0.5 M N_2H_4 electrolyte, a remarkably low cell voltage of only 79 mV was required to achieve a current density of 10 mA cm^{-2} (Fig. 9(a)). The outstanding performance is rooted in a synergistic adsorption mechanism between the Pt and Ni dual sites, as demonstrated by the theoretical calculations in Fig. 9(b-d). Specifically, the Pt sites preferentially adsorb and activate H_2O molecules, while the Ni sites favor the adsorption of N_2H_4 molecules. This complementary adsorption pattern optimizes the reaction pathway and substantially lowers the energy barrier of the overall RDS.

Beyond enhancing intrinsic activity, the anionic-cationic co-doping strategy also demonstrates a significant positive impact on improving the electrochemical durability of electrocatalysts[102, 103]. For instance, Qiu et al. [104] fabricated a hybrid electrocatalyst of Fe and P co-doped MoS_2 (Fe-P-MoS_2/CFP). As shown in Fig. 9(e), the linear sweep voltammetry (LSV) curve showed negligible decay after 3,000 cycles of cyclic voltammetry (CV) testing, demonstrating the exceptional electrocatalytic durability endowed by the synergistic Fe-P co-doping. Mechanistic studies revealed that the strong electronic interaction between Fe, P, and the MoS_2 matrix effectively modulates the local electron density and alters the electronic structure of Mo and S. This electronic-level regulation induces additional p-orbital characteristics at the S sites, which optimizes the hydrogen adsorption/desorption ΔG_{*H} and concurrently stabilizes the active centers. Consequently, Fe-P-MoS_2/CFP exhibits superior long-term operational stability under acidic conditions compared to its solely Fe-doped counterpart (Fe-MoS_2/CFP). In another study, the group of Zhang reported a bifunctional P and W co-doped Co_3N nanowire array (PW-Co_3N NWA/NF) [105]. This material also exhibited outstanding stability for the HzOR, with no significant degradation observed in its LSV curve after 5,000 CV cycles (Fig. 9(f)). The long-term stability assessed by chronoamperometry further confirmed this, retaining 92.3% of its initial current density after 10 h of continuous operation (Fig. 9(g)). Collectively, these studies emphasize that anionic-cationic co-doping simultaneously fine-tunes reaction energy barriers and reinforces catalyst structural stability through robust electronic interactions. This strategy provides a novel paradigm for designing electrocatalysts with simultaneously high activity and remarkable durability.

4.3 Heterogeneous interface

A heterostructure catalyst refers to a composite catalytic system comprising two or more distinct materials that form well-defined interfaces at the micro- or nanoscale[106]. At the heterojunction interface, the conduction and valence band positions differ between the two materials due to their distinct bandgap widths[107-109]. The group of Chen developed a (P-Co/Ni_3P)A_3/NF electrode using an alternating electrodeposition strategy, which features a layered heterostructure, abundant active sites, and strong interfacial interactions[110]. As shown in Fig. 10(a, b), the (P-Co/Ni_3P)A_3/NF electrode exhibits low potentials of -10 mV and -79 mV at 10 mA cm^{-2} for HER and HzOR, respectively, with Tafel slopes of 45 mV dec^{-1} and 1.8 mV dec^{-1}. Furthermore, the construction of the P-Co/Ni_3P heterostructure optimizes the Gibbs free energies of water adsorption and hydrogen adsorption during HER (Fig. 10(c, d)), while also enhancing the kinetics of the dehydrogenation step of HzOR reaction intermediates (Fig. 10(e)). These synergistic effects collectively improve the

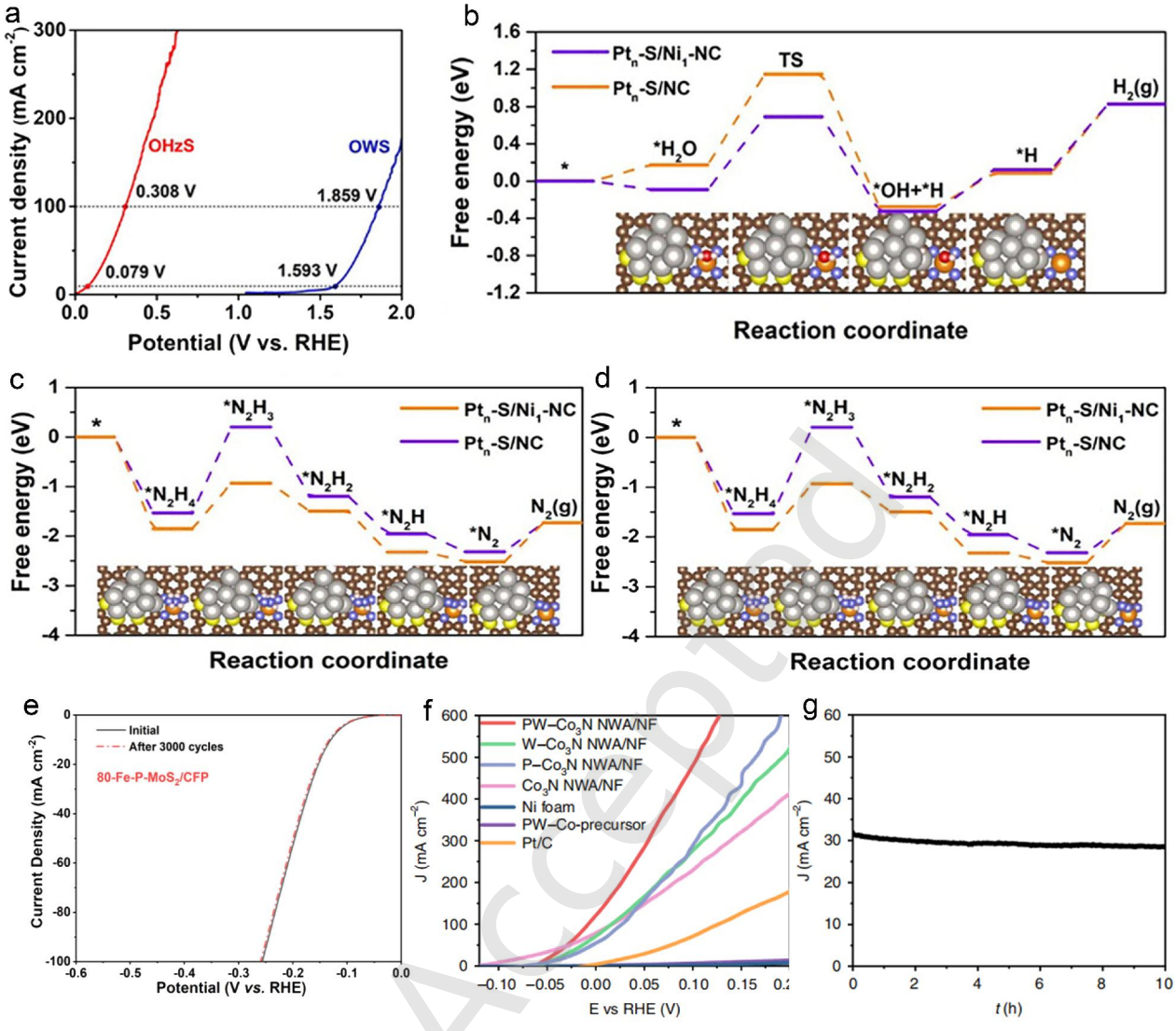

Figure 9. Co-doping strategies for hydrazine-assisted hydrogen production. (a) Comparison of LSV for OHzS and OWS using Pt_n-S/Ni_1-NC as both the cathode and anode. (b)Free energy diagrams of HER at Pt_n-S/Ni_1-NC and Pt_n-S/NC surfaces, and the adsorption configuration of the intermediate on Pt_n-S/Ni_1-NC in the inset. (c,d) Free energy diagrams of HzOR at Pt_n-S/Ni_1-NC and Pt_n-S/NC surfaces, and the adsorption configuration of the intermediate on Pt_n-S/Ni_1-NC in the inset. Reprinted with permission from Ref [101], © John Wiley and Sons 2025. (e) LSV curves of 80-Fe-P-MoS_2/CFP before and after 3000 cycles. Reprinted with permission from Ref [104], © John Wiley and Sons 2024. (f) LSV curves of different Catalysts. (g) The chronoamperometric test recorded at working potential of -40 mV. Reprinted with permission from Ref [105], © Springer Nature 2020.

bifunctional electrocatalytic performance for both HER and HzOR. Similarly, a heterostructure catalyst consisting of CoP and Ni_2P on nickel foam (CoP/Ni_2P@NF) was fabricated via electrodeposition[111]. When integrated into a hybrid electrolysis system with HER as the cathode and HzOR as the anode, the system required only 1.34 V to achieve a current density of 100 mA cm^{-2} (Fig. 10(f)). This represents a significant reduction in energy consumption compared to conventional water electrolysis, highlighting its high energy efficiency. In another study, the group of Zhang successfully achieved synergistic interfacial engineering and chemical substitution by constructing molybdenum-doped Ni_3N/Ni heterostructured porous nanosheets (Mo-Ni_3N/Ni/NF) [112]. As shown in Fig.10(g, h)，this catalyst demonstrated excellent performance under alkaline conditions, achieving a potential of 0.3 mV for HzOR and an overpotential of 45 mV for HER at 10 mA cm^{-2}.

Heterostructures serve as a common platform for generating built-in electric fields, which play a critical role in electrocatalysis[113, 114]. Yan et al. [115] reported a needle-like Ru/CoP heterostructure as a bifunctional electrocatalyst, in which the interfacial interaction induced by the built-in electric field between Ru nanoparticles and CoP nanosheets effectively modulates the catalytic behavior. A schematic diagram of this model is presented in Fig. 11(a). This interfacial engineering optimizes the adsorption of intermediates, weakens the strong adsorption of active hydrogen species on Ru sites, and enhances hydrogen coverage on CoP via hydrogen spillover, thereby improving HER performance. Simultaneously, it promotes the adsorption and subsequent dehydrogenation of N_2H_4, enhancing HzOR activity. Similarly, Pt nanoparticles were coupled with oxygen vacancy-rich $NiMoO_4$ to form a Pt@NMO-N_2 heterostructure[116]. *In situ* Raman spectroscopy (Fig. 11(b-d)) showed that with increasing potential, the ν_3 band intensity drops more quickly in Pt@NMO-N_2 compared to NMO-N_2. This band corresponds to O-H stretches from inactive water. This phenomenon

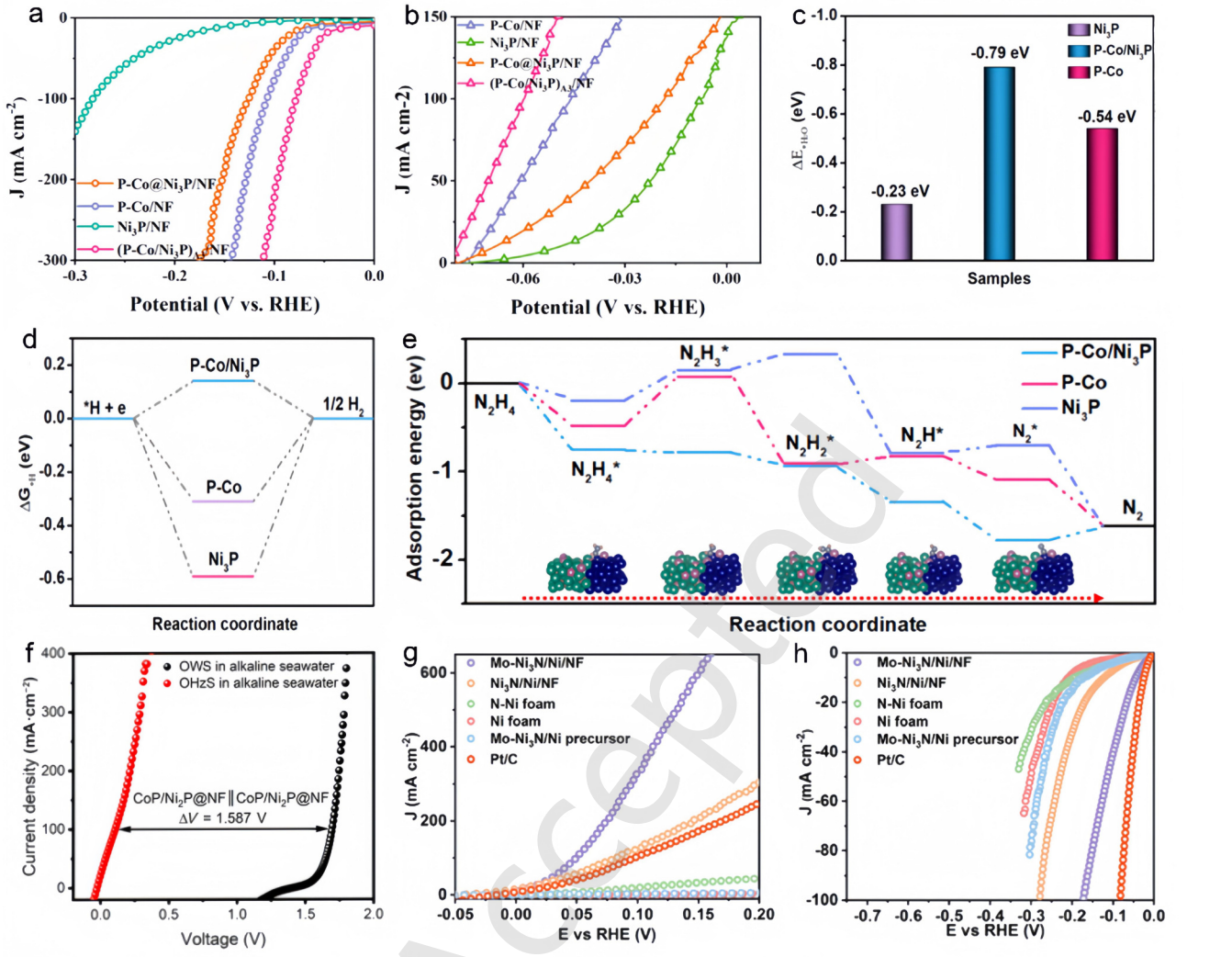

Figure 10. Heterostructure engineering for hydrazine-assisted hydrogen production. (a, b) LSV curves of catalyst samples. (c) Calculated adsorption energy of H_2O molecule and (d) calculated free energy of *H intermediate on the surface of P-Co, P-Co/Ni_3P, and Ni_3P HER materials. (e) Reaction pathways and free-energy diagram of P-Co, Ni_3P, and P-Co/Ni_3P for HzOR. Reprinted with permission from Ref [110], © American Chemical Society 2023. (f) A comparison between OHzS and OWS performance of CoP/Ni_2P@NF electrolyzer. Reprinted with permission from Ref [111], © Springer Nature 2024. (g, h) LSV curves of HER and HzOR for different catalysts. Reprinted with permission from Ref [112], © John Wiley and Sons 2021.

suggests that the heterointerface generates a local electric field. Due to this field, interfacial water dissociation is promoted, thereby enhancing the HER kinetics. Furthermore, DFT calculations demonstrated that oxygen vacancies significantly reduce the adsorption strength of *H on Pt sites, effectively improving the alkaline HER performance of Pt@NMO-N_2 (Fig. 11(e)). As shown in Fig. 11(f), the RDS for both Pt and Pt@NMO-Ov during HzOR is the dehydrogenation step from *NH_4 to *NH_3. However, Pt@NMO-Ov exhibits a lower energy barrier for HzOR, attributed to the synergistic effect between oxygen vacancies and interfacial components, which optimizes the adsorption and desorption of reaction intermediates and enhances the overall catalytic activity for both HER and HzOR.

4.4 Strain engineering

Strain engineering involves the introduction of stress into catalysts or the utilization of geometric effects, such as nanoscale deformations, to modulate the physicochemical properties of materials[117-120]. Appropriate strain can effectively regulate the surface electronic structure of catalysts, reduce reaction energy barriers, and enhance catalytic activity[121, 122]. The underlying mechanism originates from the lattice mismatch between two distinct metals, which induces distortion in the metal lattice structure, generating tensile or compressive strain. This, in turn, shifts the d-band center of the metal[123-125]. He et al. [126] developed a Cu/Co dual-cation co-doped Ni_2P material, successfully introducing compressive lattice strain. The Cu_1Co_2-Ni_2P bifunctional catalyst with a compressive strain of 3.62% exhibited the most significant enhancement in both HzOR and HER activities, requiring only 0.39 V cell voltage to achieve a current density of 100 mA cm^{-2} in a hydrazine-assisted water splitting system. As shown in Fig.12(a), when the compressive strain reaches 3.62%, the corresponding d-band center is closest to the Fermi level, indicating that strain effects can effectively promote electron transfer and optimize the d-band center position. Fig. 12(b) demonstrates that Ni_2P with optimal compressive strain exhibits the lowest N_2H_4 adsorption energy, and the dehydrogenation step becomes a thermodynamically spontaneous process, significantly enhancing HzOR activity.

4.5 Single-atom catalysts

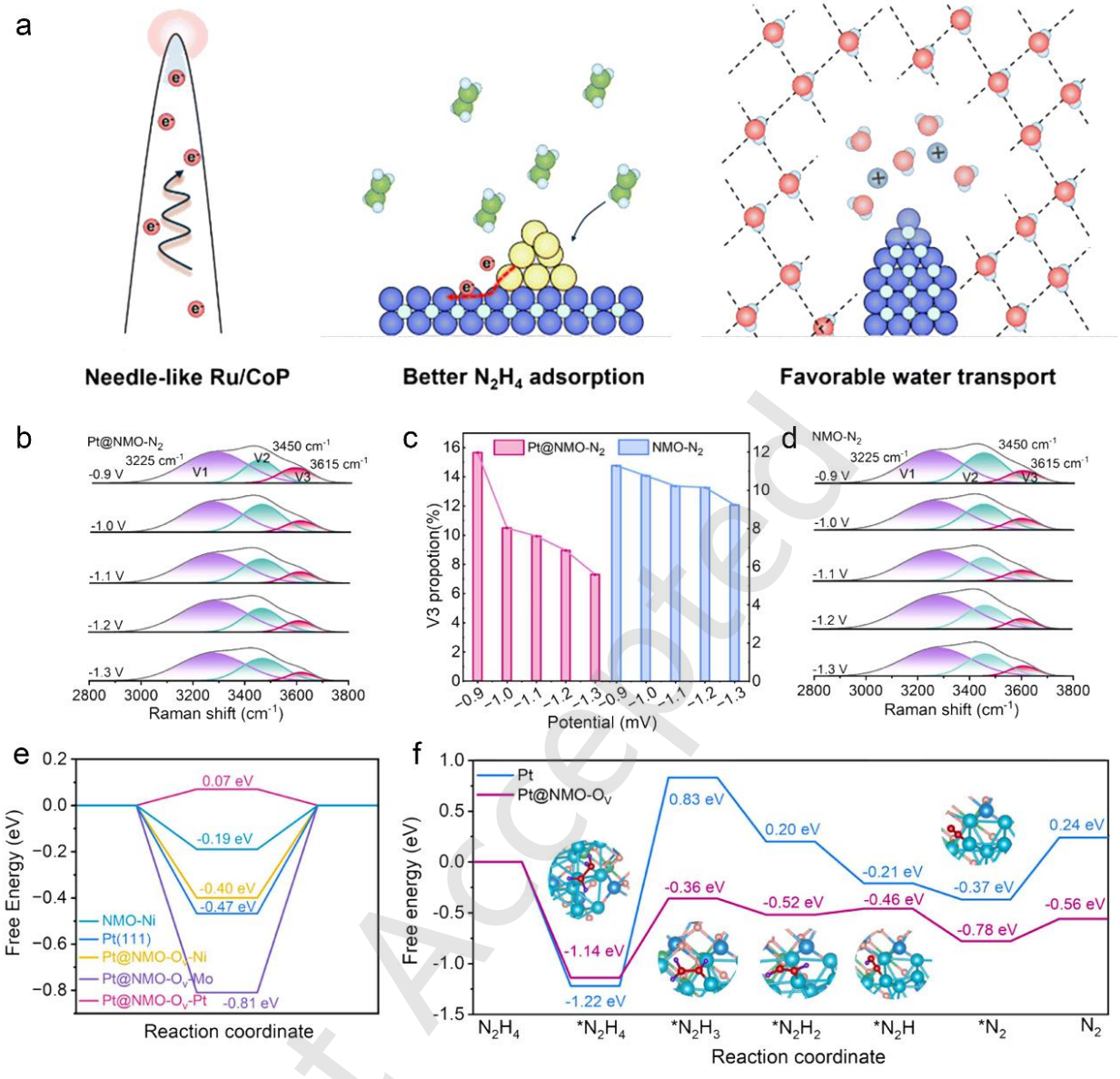

Figure 11. Built-in electric field effects in heterostructures for hydrazine-assisted hydrogen production. (a) Schematic diagram of dual-electric-field enhancement mechanism for HER and HzOR. Reprinted with permission from Ref [115], © Royal Society of Chemistry 2025. (b-d) *In situ* Raman spectra of Pt@NMO-N_2 and NMO-N_2 at different applied potentials, and the trend of the proportion of free water in the prepared catalysts with different potentials. (e) Calculated the Gibbs free energy of *H adsorption. (f) The Gibbs free energy of HzOR on the Pt@NMO-O_v and Pt. Reprinted with permission from Ref [116], © Elsevier 2025.

In recent years, Single-atom catalysts (SACs) have demonstrated outstanding performance in catalysis due to their unique maximum atom utilization efficiency[127-131]. Yuan et.al [132] successfully synthesized Ni SACs rich in Ti defects supported on a Ti_3C_2Tx Maxene substrate (Ni SACs/$Ti_3C_2T_x$). With an optimal Ni loading of 2.93 wt%, this catalyst exhibited an ultra-low onset potential of 0.03 V versus RHE and excellent HzOR stability. Li et.al [133] designed a Ru single-atom catalyst supported on a NiCoP substrate with atomically dispersed Ni(Co)-Ru-P interfacial sites. A two-electrode electrolyzer based on the OHzS reaction using this catalyst demonstrated superior activity, achieving a record high current density of 522 mA cm^{-2} at a voltage of 0.3 V. As shown in Fig. 12(c), the Faradaic efficiency obtained was close to 100%. Ma et al. [134] reported a Ru single-atom catalyst anchored on sulfur vacancies of WS_2 nanosheets via sulfidation and constant-current deposition, supported on carbon cloth (CC@WS_2/Ru SAs). Ru SAs possess high surface free energy, which leads to a tendency for aggregation. However, they can be effectively anchored at the vacancies of WS_2. This anchoring effect stabilizes the isolated Ru SAs and prevents their aggregation. As shown in Fig. 12(d), the high HER activity stems from a synergy between Ru SAs and S-edge sites in the alkaline medium. Specifically, water molecules preferentially adsorb and dissociate with low barrier on Ru sites to form OH^- and H. Concurrently, H_2 formation proceeds at adjacent S-edge sites via the combination of another H (or H_2O) and electrons, a step that nears the thermodynamic potential. Meanwhile, the Ru SAs active sites can promote the dehydrogenation process and reduce the free energy of the RDS in HzOR. As seen, the catalytic behavior of single-atom catalysts can be finely modified by the single-atom catalyst-support interface[135]. Rational design of such interface can be achieved through defect control, coordination tailoring, or support selection, which tune the

d- band center, local coordination environment of the active sites and the adsorption/desorption energetics of key intermediates, offering a powerful strategy to enhance the catalytic performance of SACs for bifunctional HER and HzOR.[136]

To summarize the different effects of interface engineering approaches on the performance of hydrazine oxidation for hydrogen production, Table 1compiles recent individual and synergistic strategies in interface regulation.

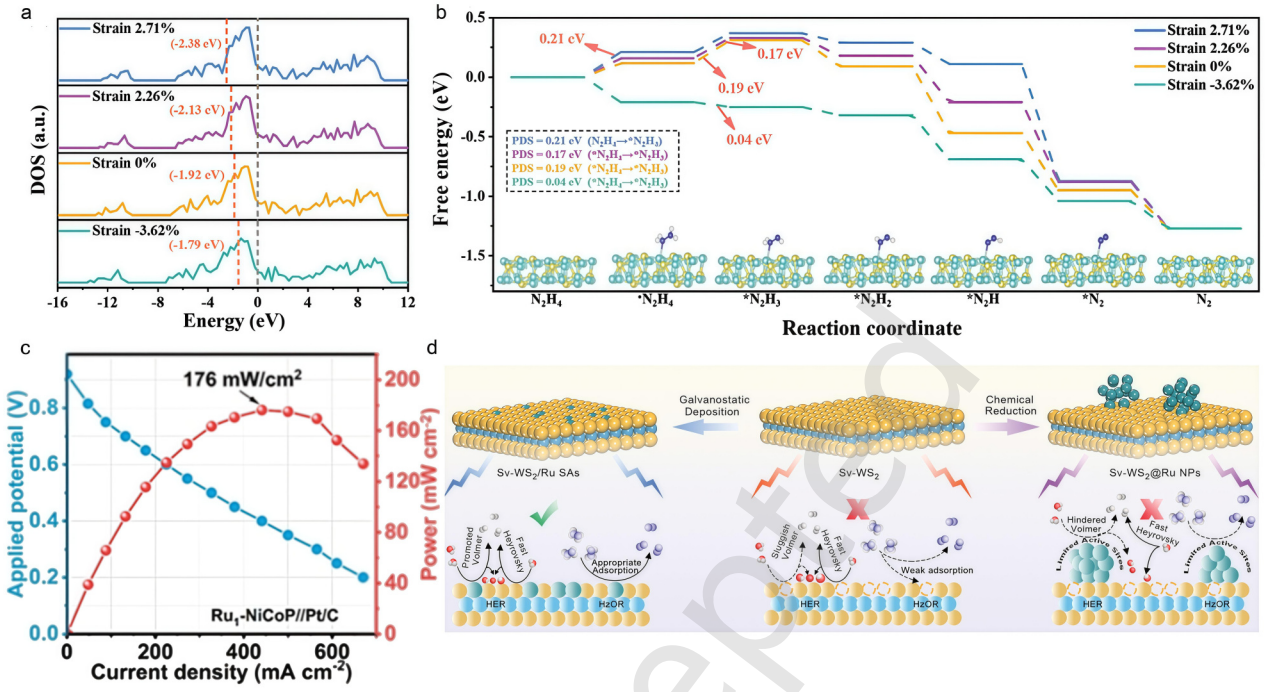

Figure 12. Strain engineering and single-atom catalysts for hydrazine-assisted hydrogen production. (a) Density of states of the comparison samples with different strains. (b) Free energy profiles of corresponding intermediates of HzOR. Reprinted with permission from Ref [126], © John Wiley and Sons 2023. (c) Discharge polarization curve and power density plot of DHzFC with Ru_1-NiCoP anode and Pt/C cathode. Reprinted with permission from Ref [135], © John Wiley and Sons 2023. (d) Schematic illustration of the proposed alkaline HER and HzOR mechanism on S_v-WS_2, S_v-WS_2@Ru NPs, and S_v-WS_2/Ru SAs. Reprinted with permission from Ref [136], © John Wiley and Sons 2022.

Table 1. Performance summary of HzOR under different interface regulations.

Catalyst	Methods	N_2H_4 Concentration (M)	Electrolyte	Overpotential (mV)	Two-electrode setup (V)	Stability (h)	Ref.
Ni SACs / Ti_3C_2Tx	Vacancy Defect	0.1	1 M KOH	30 at onset potential	--	---	[134]
dB-MOF	Defect	0.2	1 M KOH	466 at 1 mA cm^{-2}	--	20 at 0.8 V vs RHE	[137]
Ru/α-MnO_2	Vacancy Defect Doping	0.5	0.05 M H_2SO_4	166 at 10 mA cm^{-2}	0.254 at 10 mA cm^{-2}	200 at 10 mA cm^{-2}	[138]
Fe-doped CoS_2	Doping	0.1	1 M KOH	0.129 at 100 mA cm^{-2}	0.26 at 100 mA cm^{-2}	40 at 100 mA cm^{-2}	[139]
W-O-CoP/NF	Doping	0.1	1 M KOH	68 at 1000 mA cm^{-2}	0.165 at 100 mA cm^{-2}	---	[140]
P/Fe-$NiSe_2$	Doping	0.7	1 M KOH	200 at 100 mA cm^{-2}	--	100 at 100 mA cm^{-2}	[141]
W-Ni_3N	Doping Strain Engineering	1	1 M KOH	81 at 100 mA cm^{-2}	0.41 at 100 mA cm^{-2}	450 at 50 mA cm^{-2}	[142]
Cu_1Co_2-Ni_2P/NF	Doping Strain Engineering	0.1	1 M KOH	-52 at 10 mA cm^{-2}	0.16 at 10 mA cm^{-2}	20 at 20 mA cm^{-2}	[126]
Ni_3N-Co_3N PNAs/NF	Heterogeneous Interface	0.1	1 M KOH	-88 at 10 mA cm^{-2} 200 at 1000 mA cm^{-2}	0.071 at 10 mA cm^{-2}	20 at 25 mA cm^{-2}	[143]
CoN-Co_2N@NF	Heterogeneous Interface	0.1	1 M KOH	-26 at 10 mA cm^{-2}	0.053 at 10 mA cm^{-2}	50 at 220 mV	[144]
Mo-Ni_3N /Ni/NF	Doping Heterogeneous Interface	0.1	1 M KOH	-0.3 at 10 mA cm^{-2}	0.055 at 10 mA cm^{-2}	10 at 50 mA cm^{-2}	[112]

5. Conclusions and perspectives

This review systematically elucidates the critical role of interfacial engineering in advancing hydrazine oxidation-assisted water splitting systems for hydrogen production. It is demonstrated that precisely designed interfaces are powerful tools for modulating the adsorption behavior of key reaction intermediates. This capability enables the simultaneous enhancement of HzOR selectivity, the improvement of intrinsic HER activity, and a significant boost in catalyst stability under high current density operation interfacial engineering has thus been established as a vital bridge connecting atomic-scale configurations to macroscopic catalytic performance. It provides a feasible pathway toward realizing efficient, energy-saving, and stable hydrogen production via this promising technology. Nevertheless, despite tremendous progress witnessed in recent years, further researches in the following categories are envisioned to be of importance for advancing the implementation of interfacial engineering.

(1) **System Expansion** While hydrazine-assisted water splitting offers an effective electrochemical route for treating hydrazine-containing wastewater alongside hydrogen generation, it represents just one example of a thermodynamically favorable anode reaction. It remains essential to explore other innovative integrated systems. Future efforts should be directed toward coupling hydrogen production with processes like biomass conversion, waste plastic valorization, and pollutant degradation, thereby promoting broader sustainable development goals.

(2) **Mechanistic Understanding** Advancing the practical application of this technology necessitates a deeper, more intuitive understanding of reaction mechanisms at engineered interfaces. Developing and employing advanced *in situ/operando* characterization techniques is imperative to visually monitor interfacial processes and track the dynamic evolution of intermediates in real time. Uncovering the intrinsic relationship between potential-dependent interface reconstruction and reaction pathways will provide crucial theoretical guidance for designing highly stable and active catalysts.

(3) **Integration of Machine Learning** Machine learning (ML) offers a transformative approach for catalysis research. It can accelerate the discovery of optimal interfacial structures through high-throughput virtual screening and deepen the fundamental understanding of catalytic mechanisms. By training models on established experimental and theoretical datasets, ML can decipher the complex, non-linear relationships—often hidden from conventional models—between interface structure, composition, and performance. This allows for the systematic identification of key performance descriptors, providing quantitative guidelines for the rational design of next-generation interfacial catalysts and moving beyond traditional trial-and-error methods.

(4) **Path to Industrialization** To bridge the gap between laboratory research and practical application, future catalyst development must target high efficiency, exceptional durability, and low cost at industrially relevant current densities (e.g., >500 mA cm^{-2}). Research should focus on designing cost-effective, high-performance bifunctional catalysts. Surface and interface engineering strategies must be employed to synergistically enhance not only catalytic activity but also charge transport capabilities and long-term operational stability, making the industrial-scale deployment of hydrazine-assisted hydrogen production a tangible reality.

Data availability

Not applicable.

Acknowledgements

The authors thank the financial supports from the Hebei Science Foundation (B2025203050, B2025203032) NSFC(22576176)> J Wang and A. Rauf are grateful for the finacial supporte from Yanshan University (2025LGGH008).

Declaration of competing interest

All the contributing author(s) report(s) no conflict of interests in this work.

Author contribution statement

W. W.: Date collection and curation, Investigation, writing manuscript. Y. L.: Data curation. Syed Awais Ahmad: Data curation. J. W.: Formal analysis, Project administration, funding acquisition, Writing-review. Ali Rauf, R. Z., and Q. Z.: Investigation. F. G.: Formal analysis. All the authors have approved the final manuscript.

Informed consent

Not applicable

Ethics statement

Not applicable

Use of AI statement

None.

References

[1] Sha, Q.; Wang, S.; Yan, L.; Feng, Y.; Zhang, Z.; Li, S.; Guo, X.; Li, T.; Li, H.; Zhuang, Z. et al. 10,000-h-stable intermittent alkaline seawater electrolysis. *Nature* **2025**, *639*, 360-367.

[2] Sun, K.; Huang, Y.; Sun, F.; Wang, Q.; Zhou, Y.; Wang, J.; Zhang, Q.; Zheng, X.; Fan, F.; Luo, Y. et al. Dynamic structural twist in metal–organic frameworks enhances solar overall water splitting. *Nat. Chem.* **2024**, *16*, 1638-1646.

[3] Zhao, K.; Xiang, N.; Wang, Y.-Q.; Ye, J.; Jin, Z.; Fu, L.; Chang, X.; Wang, D.; Xiao, H., Xu, B. A molecular design strategy to enhance hydrogen evolution on platinum electrocatalysts. *Nat. Energy* **2025**, *10*, 725-736.

[4] Li, Y.; Niu, S.; Liu, P.; Pan, R.; Zhang, H.; Ahmad, N.; Shi, Y.; Liang, X.; Cheng, M.; Chen, S. et al. Ruthenium Nanoclusters and Single Atoms on α-MoC/N-Doped Carbon Achieves Low-Input/Input-Free Hydrogen Evolution via Decoupled/Coupled Hydrazine Oxidation. *Angew. Chem. Int. Ed.* **2024**, *63*, e202316755.

[5] Wei, Z.; Ding, Y.; Shi, W.; Zhang, F.; Song, Y.; Cui, X.; Guo, Y.; Sun, L.; Jiang, Q., Zhang, B. Lanthanum-assisted lattice anchoring of iridium in Co_3O_4 for efficient oxygen evolution reaction in low-iridium water electrolysis. *Nat. Commun.* **2025**, *16*, 8145.

[6] Ahmad, M.; Hussain, M.B.; Mushtaq, M.A.; Raza, W.; Mehmood, A.; Afzal, S.; Lu, F.; Sui, Y.; Zong, K.; Wang, X. et al. Advances in Electrocatalytic Hydrogen Evolution Coupled with Alcohol and Aldehyde Oxidation: Mechanistic Insights and Economic Feasibility. *Adv. Mater.* **2025**, *37*, 2502966.

[7] Zhu, S.; Li, L.; Zan, W.; Zhang, X.; Zhang, X.; Deng, B.; Han, G., Li, Y. Strong Interactions between Flash Subnanometer Carbide Nanowires and Single-Walled Carbon Nanotubes for Catalysis. *ACS Nano* **2025**, *19*, 28945-28957.

[8] Liu, S.; Zhang, Z.; Dastafkan, K.; Shen, Y.; Zhao, C., Wang, M. Yttrium-doped NiMo-MoO_2 heterostructure electrocatalysts for

hydrogen production from alkaline seawater. *Nat. Commun.* **2025**, *16*, 773.

[9] Tian, Y.; Chen, J.-B.; Ying, J.; Tian, G.; Xiao, Y.-X.; Lu, Y.; Wu, S.-M.; Geng, W.; Shen, L., Yang, X.-Y. Homologous CoS_2 interface with directed electron transfer and strong chloridion repulsion for efficient seawater oxidation. *Sci. China Chem.* **2025**, *68*, 1869-1878.

[10] Kang, J.; Kloppenburg, J.; Sheng, J.; Xu, Z.; Meinander, K.; Jiang, H.; Lv, Z.-P.; Kauppinen, E.I.; Zhang, Q.; Chen, X. et al. Anomalous Enhancement of the Electrocatalytic Hydrogen Evolution Reaction in AuPt Nanoclusters. *ACS Catal.* **2025**, *15*, 9928-9939.

[11] Liu, J.K.; Kang, M.; Huang, K.; Xu, H.G.; Wu, Y.X.; Zhang, X.Y.; Zhu, Y.; Fan, H.; Fang, S.R.; Zhou, Y. et al. Stable Ni(II) sites in Prussian blue analogue for selective, ampere-level ethylene glycol electrooxidation. *Nat. Commun.* **2025**, *16*, 3458.

[12] Yap, F.M.; Yuan, S.; Loh, J.Y.; Wang, J.; Zeng, X., Ong, W.-J. In-Situ Probing CO Activation in Sulfur-Enhanced Paired Electrocatalysis for CO_2-to-C^{2+} Conversion with Alcohol Oxidation. *Angew. Chem. Int. Ed.* **2025**, *64*, e202513840.

[13] Song, Y.; Qian, J.; Li, S.; Zhao, Z.; Chen, H.; Zou, K.; Han, Z.; Li, Z.; Li, H.; Zhou, H. et al. Stabilizing Lattice Oxygen to Enable Durable MnO_2 Electrocatalyst for Simultaneous Acidic Hydrogen Production and Biomass Valorization. *Angew. Chem. Int. Ed.* **2025**, *64*, e202502847.

[14] Jin, Q.; Garcia-Ortiz, M.X., Árnadóttir, L. Unveiling the role of transition-metal dopants in $Ni(OH)_2$/NiOOH-catalyzed urea oxidation. *J. Catal.* **2025**, 116503.

[15] Wu, Y., Chen, P. Hybrid water electrolysis toward energy-efficient hydrogen production coupled with value-added chemical synthesis. *Green Chem.* **2026**, *28*, 3043-3072.

[16] Shi, H.; Dai, T.-Y.; Sun, X.-Y.; Zhou, Z.-L.; Wang, Y.; Zeng, S.-P.; Wang, T.-H.; Han, G.-F.; Wen, Z.; Fang, Q.-R. et al. High-Entropy Alloy/Intermetallic Compound Heterostructures for Efficient Hydrazine Oxidation-Assisted Hydrogen Production. *Adv. Mater.* **2025**, *37*, e12081.

[17] Gao, W.; Wang, C.; Wen, W.; Wang, S.; Zhang, X.; Yan, D., Wang, S. Electrochemical Hydrogen Production Coupling with the Upgrading of Organic and Inorganic Chemicals. *Adv. Mater.* **2025**, *37*, 2503198.

[18] Zhu, L.; Huang, J.; Meng, G.; Wu, T.; Chen, C.; Tian, H.; Chen, Y.; Kong, F.; Chang, Z.; Cui, X. et al. Active site recovery and N-N bond breakage during hydrazine oxidation boosting the electrochemical hydrogen production. *Nat. Commun.* **2023**, *14*, 1997.

[19] Fu, X.; Cheng, D.; Zhang, A.; Zhou, J.; Wang, S.; Zhao, X.; Chen, J.; Sautet, P.; Huang, Y., Duan, X. Ag–Ru interface for highly efficient hydrazine assisted water electrolysis. *Energy Environ. Sci.* **2024**, *17*, 2279-2286.

[20] Burshtein, T.Y.; Yasman, Y.; Muñoz-Moene, L.; Zagal, J.H., Eisenberg, D. Hydrazine Oxidation Electrocatalysis. *ACS Catal.* **2024**, *14*, 2264-2283.

[21] Zhang, D.; Jia, X.; Liu, H.; Wang, Y.; Ye, S.; Jiang, Q.; Wang, Y.; Guo, Z.; Zhang, L.; Wei, L. et al. Cloud synthesis: a global closed-loop feedback powered by autonomous AI-driven catalyst design agent. *AI Agent* **2025**, *1*, 2.

[22] Gan, T.; Tao, L.; Zhang, Z.; Zhou, A.; Chen, Y.; Li, J.; Zhang, S.; Du, S., Li, Y. Defect-Engineered $LaFeO_3$ Stabilizing Oxidized Pt Single-Atom Sites for Low-Temperature CO Oxidation. *J. Am. Chem. Soc.* **2025**, *147*, 32729-32736.

[23] Chao, T.; Xie, W.; Hu, Y.; Yu, G.; Zhao, T.; Chen, C.; Zhang, Z.; Hong, X.; Jin, H.; Wang, D. et al. Reversible hydrogen spillover at the atomic interface for efficient alkaline hydrogen evolution. *Energy Environ. Sci.* **2024**, *17*, 1397-1406.

[24] Jia, S.; Cheng, H.; Zhu, Q.; Chen, X.; Xue, C.; Deng, T.; Dong, M.; Xia, Z.; Jiao, J.; Chen, C. et al. Tuning Multi-Active Sites in Cu Catalyst via Ag/Ni Doping for Enhanced CO_2 Electroreduction to C^{2+} Products. *Angew. Chem. Int. Ed.* **2025**, *64*, e202501833.

[25] Dong, F.; Liang, X.; Zhang, Z.; Yin, H.; Wang, D.; Li, J., Li, Y. Atomic Pt Sites Anchored in the Interface between Grains on Vacancy-Enriched CeO_2 Nanosheets: One-Step Precursor Combustion Synthesis. *Adv. Mater.* **2024**, *36*, 2401055.

[26] Lu, Y.; Liu, T.; Dong, C.-L.; Yang, C.; Zhou, L.; Huang, Y.-C.; Li, Y.; Zhou, B.; Zou, Y., Wang, S. Tailoring Competitive Adsorption Sites by Oxygen-Vacancy on Cobalt Oxides to Enhance the Electrooxidation of Biomass. *Adv. Mater.* **2022**, *34*, 2107185.

[27] Zhao, Y.; Yin, P.; Yang, Y.; Wang, R.; Gong, C.; Li, J.; Guo, J.; Wang, Q., Ling, T. Converting Fe–N–C Single-atom Catalyst to a New FeNxSey Cluster Catalyst for Proton-exchange Membrane Fuel Cells. *Angew. Chem. Int. Ed.* **2025**, *64*, e202419501.

[28] Gong, H.; Chen, H.; Duan, W.; Rao, Y.; Song, A.; Wang, X.; Wang, J.; Zhang, Y., Jiao, T. ZIF-Derived Co@Fe-P Electrocatalyst With Core-Shell Structure for Efficient Oxygen Evolution Reaction. *Carbon Energy* **2025**, *7*, e70095.

[29] Long, Y.; Zhao, S.; Wang, L.; Deng, H.; Sun, T.; Jiang, J.; Liu, T.; Sun, S.; Chen, A., Zhang, H. Regulating High Electron Spin State in Co_3S_4 for Enhanced Water Splitting. *ACS Catal.* **2025**, *15*, 9845-9855.

[30] Wang, D.; Xue, J.; Ding, X.; Wei, J.; Feng, C.; Wang, R.; Ma, P.; Wang, S.; Cao, H.; Wang, J. et al. Neighboring Cationic Vacancy Assisted Adsorption Optimization on Single-Atom Sites for Improved Oxygen Evolution. *ACS Catal.* **2022**, *12*, 12458-12468.

[31] Yang, C.; Zhang, L.; Lu, Y.; Zou, Y., Wang, S. Designing efficient catalysts for electrocatalytic organic synthesis: From electronic structure to adsorption behavior. *Matter* **2024**, *7*, 456-474.

[32] Quan, L.; Jiang, H.; Mei, G.; Sun, Y., You, B. Bifunctional Electrocatalysts for Overall and Hybrid Water Splitting. *Chem. Rev.* **2024**, *124*, 3694-3812.

[33] Hao, C.; Zhang, X.; Zhang, X.; Zhang, X.; Gao, M.; Pan, H., Sun, W. Interfacial Catalysis Engineering of Solid Electrolyte Interphase Toward High-Performance Batteries. *Small* **2025**, *21*, e09725.

[34] Tian, Y.; Xu, L.; Li, M.; Yuan, D.; Liu, X.; Qian, J.; Dou, Y.; Qiu, J., Zhang, S. Interface Engineering of CoS/CoO@N-Doped Graphene Nanocomposite for High-Performance Rechargeable Zn–Air Batteries. *Nano-Micro Lett.* **2020**, *13*, 3.

[35] Yun, Q.; Ge, Y.; Shi, Z.; Liu, J.; Wang, X.; Zhang, A.; Huang, B.; Yao, Y.; Luo, Q.; Zhai, L. et al. Recent Progress on Phase Engineering of Nanomaterials. *Chem. Rev.* **2023**, *123*, 13489-13692.

[36] Wu, W.; Yang, S.; Qian, H.; Zhang, L.; Peng, L.; Li, L.; Liu, B., Wei, Z. Interface engineering of advanced electrocatalysts toward alkaline hydrogen evolution reactions. *Chin. J. Catal.* **2024**, *66*, 1-19.

[37] Zhang, Y.; Lin, Y.; Duan, T., Song, L. Interfacial engineering of heterogeneous catalysts for electrocatalysis. *Mater. Today* **2021**, *48*, 115-134.

[38] Li, Z.; Li, B.; Yu, M.; Yu, C., Shen, P. Amorphous metallic ultrathin nanostructures: A latent ultra-high-density atomic-level catalyst for electrochemical energy conversion. *Int. J. Hydrog. Energy* **2022**, *47*, 26956-26977.

[39] Yang, Y.; Peltier, C.R.; Zeng, R.; Schimmenti, R.; Li, Q.; Huang, X.; Yan, Z.; Potsi, G.; Selhorst, R.; Lu, X. et al. Electrocatalysis in Alkaline Media and Alkaline Membrane-Based Energy Technologies. *Chem. Rev.* **2022**, *122*, 6117-6321.

[40] Wang, L.; Lv, X.-W.; Wang, H.-Y.; Ren, J.-T.; Feng, Y.; Sun, M., Yuan, Z.-Y. Rational d-Orbitals Modulation for Tailoring Co_2P Interfacial Adsorption Behavior: Boosting Alkaline Hydrogen Evolution. *Adv. Energy Mater.* **2025**, *15*, e04036.

[41] Li, P.; Jiang, Y.; Hu, Y.; Men, Y.; Liu, Y.; Cai, W., Chen, S. Hydrogen bond network connectivity in the electric double layer dominates the kinetic pH effect in hydrogen electrocatalysis on Pt. *Nat. Catal.* **2022**, *5*, 900-911.

[42] Su, H.-L.; Liao, W.; Mo, S.-X.; Wang, H.; Cao, Y.; Yu, H., Wang, H.-F. Decoupling Volmer and Tafel Steps via Dual-Site Interface Engineering in Ni/$MoBT_x$ for Efficient Hydrogen Electrocatalysis. *Adv. Funct. Mater.* **2025**, *35*, e18373.

[43] Chen, D.; Bai, H.; Zhu, J.; Wu, C.; Zhao, H.; Wu, D.; Jiao, J.; Ji, P., Mu, S. Multiscale Hierarchical Structured NiCoP Enabling Ampere-Level Water Splitting for Multi-Scenarios Green Energy-to-Hydrogen Systems. *Adv. Energy Mater.* **2023**, *13*, 2300499.

[44] Lin, Y., Ou, P. From descriptors to machine learning interatomic potentials: a review of AI-accelerated electrocatalyst design. *AI Agent* **2025**, *1*, 3.

[45] Parsons, R. The rate of electrolytic hydrogen evolution and the heat of adsorption of hydrogen. *Trans. Faraday Soc.* **1958**, *54*, 1053-1063.

[46] Nørskov, J.K.; Bligaard, T.; Logadottir, A.; Kitchin, J.R.; Chen, J.G.; Pandelov, S., Stimming, U. Trends in the Exchange Current for Hydrogen Evolution. *J. Electrochem. Soc.* **2005**, *152*, J23.

[47] Sebastián-Pascual, P.; Herzog, A.; Zhang, Y.; Shao-Horn, Y., Escudero-Escribano, M. Electrolyte effects in proton–electron transfer reactions and implications for renewable fuels and chemicals synthesis. *Nat. Catal.* **2025**, *8*, 986-999.

[48] Zhao, C.; Wang, J.; Gao, Y.; Zhang, J.; Huang, C.; Shi, Q.; Mu, S.; Xiao, Q.; Huo, S.; Xia, Z. et al. D-Orbital Manipulated Ru Nanoclusters for High-Efficiency Overall Water Splitting at Industrial-Level Current Densities. *Adv. Funct. Mater.* **2024**, *34*, 2307917.

[49] Cao, H.; Wang, Q.; Zhang, Z.; Yan, H.-M.; Zhao, H.; Yang, H.B.; Liu, B.; Li, J., Wang, Y.-G. Engineering Single-Atom Electrocatalysts for Enhancing Kinetics of Acidic Volmer Reaction. *J. Am. Chem. Soc.* **2023**, *145*, 13038-13047.

[50] Zhao, X.; Zheng, H.; Sun, H.; Chen, M.; Wang, B.; Lu, Q.; Xiao, B.; Zhou, T.; Li, D.; Qiu, G. et al. Restructuring Hydrogen Bond Networks and Enhancing Dehydrogenation Kinetics for Efficient Hydrazine Oxidation-Assisted Electrolytic Hydrogen Production. *Adv. Energy Mater.* **2025**, *15*, e04983.

[51] Wang, H.-Y.; Zhai, S.; Wang, H.; Yan, F.; Ren, J.-T.; Wang, L.; Sun, M., Yuan, Z.-Y. Taking Advantage of Potential Coincidence Region: Insights into Gas Production Behavior in Advanced Self-Activated Hydrazine-Assisted Alkaline Seawater Electrolysis. *ACS Nano* **2024**, *18*, 19682-19693.

[52] Li, G.; Zhang, H., Han, Y. Applications of Transmission Electron Microscopy in Phase Engineering of Nanomaterials. *Chem. Rev.* **2023**, *123*, 10728-10749.

[53] Song, K.; Liu, L.; Zhang, D.; Hautzinger, M.P.; Jin, S., Han, Y. Atomic-Resolution Imaging of Halide Perovskites Using Electron Microscopy. *Adv. Energy Mater.* **2020**, *10*, 1904006.

[54] Qiu, L.; Tian, F.; He, L.; Li, M.; Lin, F.; Li, L.; Ren, X.; Wu, F.; Li, L.; Zhang, T. et al. Robust Interfacial Hydrogen-Bond Network on Positively Charged Ru-N-Ni Dual Sites Boosts Alkaline Hydrogen Electrocatalysis. *Adv. Mater.* **2025**, *37*, e12568.

[55] Liang, Z.; Shen, D.; Wei, Y.; Sun, F.; Xie, Y.; Wang, L., Fu, H. Modulating the Electronic Structure of Cobalt-Vanadium Bimetal Catalysts for High-Stable Anion Exchange Membrane Water Electrolyzer. *Adv. Mater.* **2024**, *36*, 2408634.

[56] Yao, T.; Yang, Y.; Yan, Y.; Ou, X.; Li, M.; Wang, C.; Li, W.; Du, C.; Shao, X.; Gao, Z. et al. Knowledge-extractor: a self-evolving scientific framework for hydrogen energy research driven by AI agents. *AI Agent* **2025**, *1*, 7.

[57] Yin, J.; Jin, J.; Lu, M.; Huang, B.; Zhang, H.; Peng, Y.; Xi, P., Yan, C.-H. Iridium Single Atoms Coupling with Oxygen Vacancies Boosts Oxygen Evolution Reaction in Acid Media. *J. Am. Chem. Soc.* **2020**, *142*, 18378-18386.

[58] Gao, T.; Gu, J.; Yang, C.; Wang, R.; Wang, C.; Zhang, P.; Li, J.; Zheng, X.; Fan, Y.; Yang, P. et al. Strain-Engineered Rh Single Atoms on Curved WS_2 for Hydrogen Production and Coupled Photochemical Water Splitting. *J. Am. Chem. Soc.* **2025**, *147*, 25385-25396.

[59] Yang, Y.; Hao, J.; Lyu, C.; Zheng, J.; Yuan, Y.; Wang, C.; Li, K.; Yang, H.Y., Pang, X. Electron Islands-Induced Interface Engineering in FeP@NiCoP/Mo_4P_3 for Efficient Hydrogen Evolution Catalysis. *Adv. Funct. Mater.* **2025**, *35*, 2507225.

[60] Timoshenko, J., Roldan Cuenya, B. In Situ/Operando Electrocatalyst Characterization by X-ray Absorption Spectroscopy. *Chem. Rev.* **2021**, *121*, 882-961.

[61] Yang, Y.; Pang, D.; Wang, C.; Fu, Z.; Liu, N.; Liu, J.; Wu, H.; Jia, B.; Guo, Z.; Fan, X. et al. Vacancy and Dopant Co-Constructed Active Microregion in Ru–MoO_{3-x}/Mo_2AlB_2 for Enhanced Acidic Hydrogen Evolution. *Angew. Chem. Int. Ed.* **2025**, *64*, e202504084.

[62] Jian, J.; Qiao, Y.; Chen, F.; Liu, C.; Liu, W.; Li, Z.; Pi, M.; Li, Z., Zou, Z. Local charge density regulation of NiP_2 nanosheets via Ru doping for electrocatalytic urea oxidation. *Appl. Catal. B: Environ.* **2025**, *374*, 125390.

[63] Liu, X.; Wang, X.; Mao, C.; Qiu, J.; Wang, R.; Liu, Y.; Chen, Y., Wang, D. Ligand-Hybridization Activates Lattice-Hydroxyl-Groups of $NiCo(OH)_x$ Nanowires for Efficient Electrosynthesis. *Angew. Chem. Int. Ed.* **2024**, *63*, e202408109.

[64] Pang, K.; Tang, Y.; Qiu, C.; Zhang, M.; Tayal, A.; Feng, S.; Long, C.; Wang, Y.; Chang, J.; Pang, B. et al. Redirecting configuration of atomically dispersed selenium catalytic sites for efficient hydrazine oxidation. *Matter* **2024**, *7*, 655-667.

[65] Chen, K., Tong, Y. Electrocatalytic upgrading of polyethylene terephthalate: mechanisms, catalyst design, and paired electrolysis applications. *Inorganic Chemistry Frontiers* **2026**, *13*, 1797-1820.

[66] Yuan, S.-X.; Su, K.; Feng, Y.-X.; Dong, G.-X.; Zhang, M., Lu, T.-B. Titanium vacancy-tuned Fermi level shifting amplifies the built-in electric field in perovskite/TiO_2 heterojunctions for boosting charge separation and CO_2 photoreduction. *Sci. China Chem.* **2026**, *69*, 1-8.

[67] Qin, Z.; Zhang, P.; Chang, B.; Bao, L.; Wang, Q.; Zhou, W.; Zeng, D., Lu, X. Water-induced defect engineering in metal-organic frameworks toward enhanced gas-sensing performance. *Sci. China Chem.* **2026**, *69*, 197-205.

[68] Chen, X.; Wang, J.; Patel, S.B.; Ye, S.; Wu, Y.; Zhou, Z.; Qiao, L.; Wang, Y.; Marinkovic, N.; Li, M. et al. Atomic dynamics of gas-dependent oxide reducibility. *Nature* **2025**, *644*, 927-932.

[69] Xu, X.; Tang, T.; Zhang, G., Guan, J. Tuning electronic structure of cobaltous nitride-manganous oxide heterojunction by N-vacancy engineering for optimizing oxygen electrocatalysis activity. *Nano Energy* **2024**, *131*, 110294.

[70] Hu, J.; Jin, L.; Kou, H.; Li, H.-J.; Xu, J.; Hu, Q.; Li, G., Wang, D. Dual-Motor Oxygen-Deficiency-Engineering Al-Doped $W_{18}O_{49-x}$ Circular Nanorod Arrays for Parts per Billion-Level Acetone Detection. *Nano Lett.* **2025**, *25*, 14131-14139.

[71] Wang, M.; Wang, W.; Zhang, Y.; Liu, X.; Gao, L.; Jing, X.; Hu, Z.; Lu, J., Ni, Z. Controllable n-type doping in WSe_2 monolayer via construction of anion vacancies. *Chin. Chem. Lett.* **2021**, *32*, 3118-3122.

[72] Wang, B.; Huang, F.; Wu, H.; Xu, Z.; Wang, S.; Han, Q.; Liu, F.; Li, S., Zhang, H. Enhanced interfacial polarization of defective porous carbon confined CoP nanoparticles forming Mott-Schottky heterojunction for efficient electromagnetic wave absorption. *Nano Res.* **2023**, *16*, 4160-4169.

[73] Koley, P.; Shit, S.C.; Yoshida, T.; Jampaiah, D.; Ariga-Miwa, H.; Uruga, T.; Kaishyop, J.; Hosseinnejad, T.; Periasamy, S.; Gudi, R.D. et al. Metal organic framework derived In_2O_3/ZrO_2 heterojunctions with interfacial oxygen vacancies for highly selective CO_2-to-methanol hydrogenation. *Nat. Commun.* **2025**, *16*, 8903.

[74] Wang, L.; Zhou, J.; Zhou, Y.; Liu, K.; Ke, L.; Li, H.; Liu, S.; Wang, X.; Zhu, W.; Li, Y. et al. Oxygen Vacancy-Mediated Oxide Pathway Mechanism in Proton-Exchange Membrane Water Electrolysis. *Adv. Funct. Mater.* **2025**, *35*, e16646.

[75] Guo, Y.; Xu, Y., Chen, P. Ampere-level glycerol electrooxidation enabled by oxygen vacancy-riched crystalline/amorphous Co_3O_{4-x}/ZrO_{2-x} Heterointerface. *J. Colloid Interface Sci.* **2025**, *699*, 138292.

[76] Xu, X.; Chen, H.-C.; Li, L.; Humayun, M.; Zhang, X.; Sun, H.; Jia, J.; Xu, C.; Bououdina, M.; Sun, L. et al. Understanding the Role of Oxygen Vacancy Defects in Iridium-Leveraged MOFs-Type Catalyst. *Adv. Funct. Mater.* **2024**, *34*, 2408823.

[77] Sun, R.; Bai, Y.; Bai, Z.; Peng, L.; Luo, M.; Qu, M.; Gao, Y.; Wang, Z.; Sun, W., Sun, K. Phosphorus Vacancies as Effective Polysulfide Promoter for High-Energy-Density Lithium–Sulfur Batteries. *Adv. Energy Mater.* **2022**, *12*, 2102739.

[78] Liu, T.; Lin, R.; Chen, Y.L.C.; Huang, Q.; Sun, Y.; Huang, S.; Amiinu, I.S., Pu, Z. Ultrafast carbothermal shock synthesis of transition metal phosphides in air for highly efficient hydrogen evolution reaction. *Chin. Chem. Lett.* **2025**, *36*, 111312.

[79] Wei, X.; Zhang, S.; Lv, X.; Dai, S.; Wang, H., Huang, M. Local-reconstruction enables cobalt phosphide array with bifunctional hydrogen evolution and hydrazine oxidation. *Appl. Catal. B: Environ.* **2024**, *345*, 123661.

[80] Chi, J.; Guo, L.; Mao, J.; Cui, T.; Zhu, J.; Xia, Y.; Lai, J., Wang, L. Modulation of Electron Structure and Dehydrogenation Kinetics of Nickel Phosphide for Hydrazine-Assisted Self-Powered Hydrogen Production in Seawater. *Adv. Funct. Mater.* **2023**, *33*, 2300625.

[81] Zheng, Y.; Zhang, H.; Xiong, J.; Zhao, Z.; Zhang, D., Chen, L. Anion-induced vacancy enhances Co_3Se_4/Fe_3Se_4 heterostructures for high-efficiency hydrogen production. *Fuel* **2024**, *360*, 130651.

[82] Alemayehu, D.D.; Tsai, M.-C.; Tsai, M.-H.; Yang, C.-C.; Chang, C.-C.; Chang, C.-Y.; Moges, E.A.; Lakshmanan, K.; Nikodimos, Y.; Su, W.-N. et al. Heterogeneous Interfaces of Ni_3Se_4 Nanoclusters Decorated on a Ni_3N Surface Enhance Efficient and Durable Hydrogen Evolution Reactions in Alkaline Electrolyte. *J. Am. Chem. Soc.* **2025**, *147*, 16047-16059.

[83] Jiang, R.; Jin, M.; Du, C.; Song, T.; Ma, X.; Zhu, Y.; Cao, C., Zou, M. Rich Se Vacancies $MoxV_{1-x}Se_2$ Nanosheets with Synergistic Optimization of Electronic and Lattice Structures for Accelerating Sulfur Redox Kinetics in Mg-S Batteries. *Adv. Energy Mater.* **2025**, *15*, e05028.

[84] Yan, W.; Ma, H.; Zhao, X.; Zhang, Y.; Vishniakov, P.; Wang, X.; Zhong, X.; Hong, Z.; Maximov, M.Y.; Song, L. et al. P and Se Binary Vacancies and Heterostructures Modulated MoP/$MoSe_2$ Electrocatalysts for Improving Hydrogen Evolution and Coupling Electricity Generation. *Small* **2023**, *19*, 2208270.

[85] Rong, J.; Zhang, J.; Wang, W.; Miao, J.; Chen, L., Cui, S. Quantum-Sized Co Nanoparticles with Rich Vacancies Enabled the Uniform Deposition of Lithium Metal and Fast Polysulfide Conversion. *Small* **2024**, *20*, 2406908.

[86] Wang, W.; Zhang, J.; Rong, J.; Chen, L., Cui, S. Quantum-sized CoP nanodots with rich vacancies: Enhanced hydrazine oxidation, hydrazine-assisted water splitting, and Zn-hydrazine battery performance through interface modulation. *J. Colloid Interface Sci.* **2025**, *680*, 214-223.

[87] Pang, Q.; Liu, J.; Zheng, C.; Wu, Y.; Yang, Y.; He, Z.; Lu, C., Xie, Y. Synergistic modulation of electronic band structures through heterogeneous cation-anion dual vacancies for efficient photocatalytic hydrogen evolution. *Sci. China Chem.* **2025**, *68*, 6103-6115.

[88] Wu, Q., Xu, Z.J. Mechanistic Insights into Cation Effects in Electrolytes for Electrocatalysis. *Angew. Chem. Int. Ed.* **2025**, *64*, e202505022.

[89] Yuan, D.; Dou, Y.; Tian, Y.; Adekoya, D.; Xu, L., Zhang, S. Robust Pseudocapacitive Sodium Cation Intercalation Induced by Cobalt Vacancies at Atomically Thin $Co_{1-x}Se_2$/Graphene Heterostructure for Sodium-Ion Batteries. *Angew. Chem. Int. Ed.* **2021**, *60*, 18830-18837.

[90] Yu, H.; Xue, S.; Gubanova, E.L.; Zhou, J.; Bautista, R.; Himmelreich, A.V., Bandarenka, A.S. Cation-Dependent Interfacial Properties Determine the Activity of Pt(111) Electrodes in Alkaline Media. *ACS Catal.* **2025**, *15*, 19721-19730.

[91] Mo, S.-X.; Su, H.-L.; Chen, J.; Liao, W.; Wang, Y.; Wang, H.; Cao, Y.; Yu, H., Wang, H.-F. Defect-Promoted Reductive Regeneration on Cobalt Catalysts Enables Efficient Dual-Pathway Hydrazine Electrooxidation. *Angew. Chem. Int. Ed.* **2025**, *64* e202514064.

[92] Jia, Z.; He, Y.; Zhang, X.; Chen, X.; Yuan, X.; Liu, L.; Fu, L.; Chen, Y.; Wang, T.; Cheng, X. et al. Amorphous phase engineering in Ni-doped MoS_2@C: synergistic structural-electronic modulation for high-energy-power sodium-ion hybrid capacitors. *Sci. China Chem.* **2025**, *68*, 1-10.

[93] Pei, S.; Wang, S.; Lu, Y.; Li, X., Wang, B. Application of metal-based catalysts for Fenton reaction: from homogeneous to heterogeneous, from nanocrystals to single atom. *Nano Res.* **2024**, *17*, 9446-9471.

[94] Dai, R.; Chen, P., Tong, Y. Engineering Interfacial Electronic Polarization in Pt@S-Co_3O_{4-x} for Superior Glycerol-Assisted Water Electrolysis. *ACS Sustainable Chem. Eng.* **2026**, *14*, 2233-2242.

[95] Wang, X.; Ma, R.; Li, S.; Xu, M.; Liu, L.; Feng, Y.; Thomas, T.; Yang, M., Wang, J. In Situ Electrochemical Oxyanion Steering of Water Oxidation Electrocatalysts for Optimized Activity and Stability. *Adv. Energy Mater.* **2023**, *13*, 2300765.

[96] Wang, J.; Li, X.; Wei, B.; Sun, R.; Yu, W.; Hoh, H.Y.; Xu, H.; Li, J.; Ge, X.; Chen, Z. et al. Activating Basal Planes of $NiPS_3$ for Hydrogen Evolution by Nonmetal Heteroatom Doping. *Adv. Funct. Mater.* **2020**, *30*, 1908708.

[97] Zhou, K.; Liu, H.; Liu, Z.; Li, X.; Wang, N.; Wang, M.; Xue, T.; Shen, Y.; Li, H.; Li, H. et al. W-Mediated Electron Accumulation in Ru−O−W Motifs Enables Ultra-Stable Oxygen Evolution Reaction in Acid. *Angew. Chem. Int. Ed.* **2025**, *64*, e202422707.

[98] Gicha, B.B.; Banti, B.F.; Molla, C.F.; Kang, H.; Goddati, M.; Khoris, I.M.; Nwaji, N.; Asgaran, S., Lee, J. Interfacial Electronic Synergism in Cobalt-Doped MoS_2-COF Heterostructures for Energy-Efficient Hydrazine-Assisted Hydrogen Production. *Small* **2025**, *21*, e08200.

[99] Li, Z.; Li, C.; Chen, J.; Xing, X.; Wang, Y.; Zhang, Y.; Yang, M., Zhang, G. Confined synthesis of MoS_2 with rich co-doped edges for enhanced hydrogen evolution performance. *J. Energy Chem.* **2022**, *70*, 18-26.

[100] Lu, Y.; Pei, C.; Li, W.; Liu, Q.; Pang, H., Yu, X. Tailoring active sites of cerium and nitrogen Co-doped rhenium disulfide for enhanced hydrogen evolution reaction. *Chin. Chem. Lett.* **2025**, *36*, 111646.

[101] Lv, Y.-K.; Wang, K.; Du, C.-X.; Huang, R.-W.; Zang, S.-Q., Peng, P. Sulfur-Stabilized Superfine Pt Clusters Synergized with Single-Atom Ni-N_4 Sites for Hydrazine Oxidation-Assisted Hydrogen Production. *Adv. Mater.* **2025**, *37*, e16082.

[102] Zheng, W.; Zhao, Y.; Jiang, K.; Xie, F.; Meng, L.; Gao, S.; Li, J.; Lan, J.; Luo, M.; Liu, L. et al. Heteroatom dopants overcome the activity-stability trade-off in RuO_2 for acidic oxygen evolution. *Nat. Commun.* **2025**, *16*, 6716.

[103] Zhang, Y.; Yang, T.; Li, J.; Zhang, Q.; Li, B., Gao, M. Construction of Ru, O Co-Doping MoS_2 for Hydrogen Evolution Reaction Electrocatalyst and Surface-Enhanced Raman Scattering Substrate: High-Performance, Recyclable, and Durability Improvement. *Adv. Funct. Mater.* **2023**, *33*, 2210939.

[104] Chiang, C.-H.; Chen, H.-T.; Chen, W.-Y.; Wang, W.-T.; Feng, S.-P., Wu, C.-G. Tin Oxide/Amphiphilic Polymer Double-Layered Hole Transporter for High-Efficiency Tin Perovskite Solar Modules. *Adv. Energy Mater.* **2024**, *14*, 2400346.

[105] Liu, Y.; Zhang, J.; Li, Y.; Qian, Q.; Li, Z.; Zhu, Y., Zhang, G. Manipulating dehydrogenation kinetics through dual-doping Co_3N electrode enables highly efficient hydrazine oxidation assisting self-powered H_2 production. *Nat. Commun.* **2020**, *11*, 1853.

[106] Luo, Y.; Zhou, H., Tong, Y. Advances in Nanostructured Catalysts for Urea-Assisted Water Splitting and Zn-Urea Batteries. *ChemSusChem* **2026**, *19*, e202502504.

[107] Shi, H.; Dai, T.-Y.; Sun, X.-Y.; Zhou, Z.-L.; Zeng, S.-P.; Wang, T.-H.; Han, G.-F.; Wen, Z.; Fang, Q.-R.; Lang, X.-Y. et al. Dual-Intermetallic Heterostructure on Hierarchical Nanoporous Metal for Highly Efficient Alkaline Hydrogen Electrocatalysis. *Adv. Mater.* **2024**, *36*, 2406711.

[108] Le, C.V.; Ju, M.; Nguyen, T.T.T.; Lee, H., Yoon, H. Hetero-layered 2D materials: Scalable preparation and energy applications. *Mater. Sci. Eng.: R: Rep.* **2025**, *163*, 100937.

[109] Yan, Z.; Gong, J.; Sun, H.; Jin, T.; Yang, D.; Gu, L.; Zhang, L.; Shen, S., Zhong, W. Heterojunction-doping synergy in strontium palladium-ruthenium oxide catalysts for efficient oxygen evolution. *Nano Res.* **2026**, *19*, 94908006.

[110] Li, K.; Zhou, G.; Tong, Y.; Ye, Y., Chen, P. Interface Engineering of a Hierarchical P-Modified Co/Ni_3P Heterostructure for Highly Efficient Water Electrolysis Coupled with Hydrazine Degradation. *ACS Sustainable Chem. Eng.* **2023**, *11*, 14186-14196.

[111] Liu, W.; Liu, W.; Hou, T.; Ding, J.; Wang, Z.; Yin, R.; San, X.; Feng, L.; Luo, J., Liu, X. Coupling Co-Ni phosphides for energy-saving alkaline seawater splitting. *Nano Res.* **2024**, *17*, 4797-4806.

[112] Liu, Y.; Zhang, J.; Li, Y.; Qian, Q.; Li, Z., Zhang, G. Realizing the Synergy of Interface Engineering and Chemical Substitution for Ni3N Enables its Bifunctionality Toward Hydrazine Oxidation Assisted Energy-Saving Hydrogen Production. *Adv. Funct. Mater.* **2021**, *31*, 2103673.

[113] Han, Y.-W.; Zhang, Y.-X.; Ye, L.; Gong, T.-J.; Lu, X.-B.; Yan, N., Fu, Y. Establishing Dual-Interface Built-In Electric Fields within Janus Heterostructures for Cooperative Photoredox Catalysis. *J. Am. Chem. Soc.* **2025**, *147*, 18637-18650.

[114] Wang, D.; Wang, S.; Zhang, H.; Cui, C.; Hao, S.; Qiu, P.; Zheng, L., Yang, Y. Tunable built-in electric field of homologous heterojunction regulated by nitrogen doped carbon to enhance water splitting. *Nano Res.* **2025**, *18*, 94907381.

[115] Ji, K.; Wang, S.; Yao, S.; Ji, Y.; Wang, G.; Ren, W.; Wang, J.; Zhang, F.; Xie, J.; Yang, Z. et al. Modeling carbon-free energy conversion systems: enhanced hydrazine-assisted hydrogen production with dual-electric-field effect on needle-like Ru/CoP catalysts. *Energy Environ. Sci.* **2025**, *18*, 4764-4774.

[116] Zhao, X.; Zheng, H.; Sun, H.; Chen, M.; Wang, B.; Lu, Q.; Xiao, B.; Zhou, T.; Li, D.; Qiu, G. et al. Interfacial component coupling effects induce electron redistribution for enhanced hydrazine-assisted hydrogen production at ampere-level current densities. *Nano Energy* **2025**, *142*, 111201.

[117] Li, Y.; Li, Y.; Zhao, Y.; Ren, Y.; Ge, Z.; Lu, J.; Wang, Q.; Feng, A.; Xiao, C., Jin, M. Strain-Engineered Noble Metal Nanocatalysts for Electrocatalytic Applications. *Adv. Mater.* **2025**, *37*, e16277.

[118] Wang, L.; Zhou, X.; Luo, Z.; Liu, S.; Yue, S.; Chen, Y., Liu, Y. Review of External Field Effects on Electrocatalysis: Machine Learning Guided Design. *Adv. Funct. Mater.* **2024**, *34*, 2408870.

[119] Zhao, Y.; Yu, H.; Tang, J.; Li, Y.; Yong, X.; Tu, X., Wang, J. Strain engineering of heterogeneous catalysts for oxygen reduction reaction. *Chin. Chem. Lett.* **2025**, *36*, 111997.

[120] Zhao, X.; Sun, Y.; Wang, J.; Nie, A.; Zou, G.; Ren, L.; Wang, J.; Wang, Y.; Fernandez, C., Peng, Q. Regulating d-Orbital Hybridization of Subgroup-IVB Single Atoms for Efficient Oxygen Reduction Reaction. *Adv. Mater.* **2024**, *36*, 2312117.

[121] Yang, X.; Wang, Y.; Tong, X., Yang, N. Strain Engineering in Electrocatalysts: Fundamentals, Progress, and Perspectives. *Adv. Energy Mater.* **2022**, *12*, 2102261.

[122] Zhang, H.; Chi, K.; Qiao, L.; Gao, P.; Li, Z.; Guo, X.; Li, Z.; Cao, D., Cheng, D. Boosting Acidic Hydrogen Evolution Kinetics Induced by Weak Strain Effect in PdPt Alloy for Proton Exchange Membrane Water Electrolyzers. *Small* **2024**, *20*, 2406935.

[123] Guo, H.; Li, L.; Chen, Y.; Zhang, W.; Shang, C.; Cao, X.; Li, M.; Zhang, Q.; Tan, H.; Nie, Y. et al. Precise Strain Tuning Boosts Electrocatalytic Hydrogen Generation. *Adv. Mater.* **2023**, *35*, 2302285.

[124] Chen, Y.; Cheng, Z.; Zhang, H.; Liang, J.; Li, J.; Bao, C.; Chen, S.; Wu,

X.; Liu, Z.; Jia, J. et al. 3D Nanoarrays Induced Compression Strain on Ultra-Thin NiOOH Optimizes H_2O Adsorption for Efficient Hydrogen and Oxygen Evolution Reactions. *Adv. Funct. Mater.* **2025**, *35*, e14027.

[125] Li, Z.; Wang, Y.; Liu, H.; Feng, Y.; Du, X.; Xie, Z.; Zhou, J.; Liu, Y.; Song, Y.; Wang, F. et al. Electroreduction-driven distorted nanotwins activate pure Cu for efficient hydrogen evolution. *Nat. Mater.* **2025**, *24*, 424-432.

[126] Feng, C.; Lv, M.; Shao, J.; Wu, H.; Zhou, W.; Qi, S.; Deng, C.; Chai, X.; Yang, H.; Hu, Q. et al. Lattice Strain Engineering of Ni_2P Enables Efficient Catalytic Hydrazine Oxidation-Assisted Hydrogen Production. *Adv. Mater.* **2023**, *35*, 2305598.

[127] Liu, X.; Zhou, Y.; Lin, J.; Xiao, X.; Wang, Z.; Jia, L.; Li, M.; Yang, K.; Fan, J.; Yang, W. et al. Directional Growth and Density Modulation of Single-Atom Platinum for Efficient Electrocatalytic Hydrogen Evolution. *Angew. Chem. Int. Ed.* **2024**, *63*, e202406650.

[128] Hei, P.; Sai, Y.; Li, W.; Meng, J.; Lin, Y.; Sun, X.; Wang, J.; Song, Y., Liu, X.-X. Diatomic Catalysts for Aqueous Zinc-Iodine Batteries: Mechanistic Insights and Design Strategies. *Angew. Chem. Int. Ed.* **2024**, *63*, e202410848.

[129] Yu, R.; Cao, X.; Zhu, C.; Chen, Q.; Yan, Z.; Jiang, B.; Mao, J., Wei, X. Asymmetric interfacial engineering regulated charge distribution on Ru/Ni-N-C sites for efficient hydrogen evolution reaction in alkaline and seawater electrolytes. *Sci. China Chem.* **2025**, *68*, 3048-3055.

[130] Shangguan, Y.; Wang, R.; Zhou, Y.; Feng, X., Chen, H. Design and engineering of single-atom catalysts for environmental remediation: Principles and structural-property relationship. *Nano Res.* **2025**. DOI: 10.26599/NR.2025.94908168.

[131] Liu, H.; Zhu, P.; Yang, D.; Zhong, C.; Li, J.; Liang, X.; Wang, L.; Yin, H.; Wang, D., Li, Y. Pd–Mn/NC Dual Single-Atomic Sites with Hollow Mesopores for the Highly Efficient Semihydrogenation of Phenylacetylene. *J. Am. Chem. Soc.* **2024**, *146*, 2132-2140.

[132] Zhou, S.; Zhao, Y.; Shi, R.; Wang, Y.; Ashok, A.; Héraly, F.; Zhang, T., Yuan, J. Vacancy-Rich MXene-Immobilized Ni Single Atoms as a High-Performance Electrocatalyst for the Hydrazine Oxidation Reaction. *Adv. Mater.* **2022**, *34*, 2204388.

[133] Hu, Y.; Chao, T.; Li, Y.; Liu, P.; Zhao, T.; Yu, G.; Chen, C.; Liang, X.; Jin, H.; Niu, S. et al. Cooperative Ni(Co)-Ru-P Sites Activate Dehydrogenation for Hydrazine Oxidation Assisting Self-powered H_2 Production. *Angew. Chem. Int. Ed.* **2023**, *62*, e202308800.

[134] Li, J.; Li, Y.; Wang, J.; Zhang, C.; Ma, H.; Zhu, C.; Fan, D.; Guo, Z.; Xu, M.; Wang, Y. et al. Elucidating the Critical Role of Ruthenium Single Atom Sites in Water Dissociation and Dehydrogenation Behaviors for Robust Hydrazine Oxidation-Boosted Alkaline Hydrogen Evolution. *Adv. Funct. Mater.* **2022**, *32*, 2109439.

[135] Guo, Y.; Liang, J.; Huang, Y.; Yang, J.; Zhang, Q.; Wang, A.; Qiao, B.; Li, J., Zhang, T. Covalent and Strong Metal – Support Interactions for Robust Single-Atom Catalysts. Acc. Chem. Res. 2025, 58, 2440-2453.

[136] Gloag, L.; Somerville, S.V.; Gooding, J.J., Tilley, R.D. Co-catalytic metal–support interactions in single-atom electrocatalysts. *Nat. Rev. Mater.* **2024**, *9*, 173-189.

[137] Guo, D.; Ding, J.; Hu, C.; Zhao, M.; Shen, K.; Chen, L., Li, Y. Creating Abundant Open Metal Sites in MOFs by Dual-Coordination Design for Enhanced Electrocatalytic Activity. *Angew. Chem. Int. Ed.* **2025**, *64*, e202515653.

[138] Yu, Z.; Si, C.; Sabaté, F.; LaGrow, A.P.; Tai, Z.; Diaconescu, V.M.; Simonelli, L.; Meng, L.; Sabater, M.J.; Li, B. et al. Defective Ru-doped α-MnO_2 nanorods enabling efficient hydrazine oxidation for energy-saving hydrogen production via proton exchange membranes at near-neutral pH. *Chem. Eng. J.* **2023**, *470*, 144050.

[139] Liu, X.; He, J.; Zhao, S.; Liu, Y.; Zhao, Z.; Luo, J.; Hu, G.; Sun, X., Ding, Y. Self-powered H_2 production with bifunctional hydrazine as sole consumable. *Nat. Commun.* **2018**, *9*, 4365.

[140] Meng, G.; Chang, Z.; Zhu, L.; Chen, C.; Chen, Y.; Tian, H.; Luo, W.; Sun, W.; Cui, X., Shi, J. Adsorption Site Regulations of [W–O]-Doped CoP Boosting the Hydrazine Oxidation-Coupled Hydrogen Evolution at Elevated Current Density. *Nano-Micro Lett.* **2023**, *15*, 212.

[141] Wang, H.-Y.; Wang, L.; Ren, J.-T.; Tian, W.-W.; Sun, M.-L., Yuan, Z.-Y. Heteroatom-Induced Accelerated Kinetics on Nickel Selenide for Highly Efficient Hydrazine-Assisted Water Splitting and Zn-Hydrazine Battery. *Nano-Micro Lett.* **2023**, *15*, 155.

[142] Qin, H.; Lin, G.; Zhang, J.; Cao, X.; Xia, W.; Yang, H.; Yuan, K.; Jin, T.; Wang, Q., Jiao, L. Enhanced Cooperative Generalized Compressive Strain and Electronic Structure Engineering in W-Ni_3N for Efficient Hydrazine Oxidation Facilitating H_2 Production. *Adv. Mater.* **2025**, *37*, 2417593.

[143] Qian, Q.; Zhang, J.; Li, J.; Li, Y.; Jin, X.; Zhu, Y.; Liu, Y.; Li, Z.; El-Harairy, A.; Xiao, C. et al. Artificial Heterointerfaces Achieve Delicate Reaction Kinetics towards Hydrogen Evolution and Hydrazine Oxidation Catalysis. *Angew. Chem. Int. Ed.* **2021**, *60*, 5984-5993.

[144] Xiong, D.; He, X.; Liu, X.; Gong, S.; Xu, C.; Tu, Z.; Wu, D.; Wang, J., Chen, Z. 1D/3D Heterogeneous Assembling Body of Cobalt Nitrides for Highly Efficient Overall Hydrazine Splitting and Supercapacitors. *Small* **2024**, *20*, 2306100.